# Arrhythmia mutations in calmodulin can disrupt cooperativity of Ca2+ binding and cause misfolding

Wang, Kaiqian; Brohus, Malene; Holt, Christian; Overgaard, Michael Toft; Wimmer, Reinhard; Van Petegem, Filip

*Published in:*
The Journal of Physiology

*DOI (link to publication from Publisher):*
10.1113/JP279307

*Publication date:*
2020

*Document Version*
Accepted author manuscript, peer reviewed version

# Arrhythmia mutations in calmodulin can disrupt cooperativity of $Ca^{2+}$ binding and cause misfolding

**Running title:** Arrhythmia mutations in calmodulin

Kaiqian Wang[1], Malene Brohus[2], Christian Holt[2], Michael Toft Overgaard[2], Reinhard Wimmer[2], Filip Van Petegem[1,*]

[1] Department of Biochemistry and Molecular Biology, Life Sciences Institute, University of British Columbia, V6T 1Z3 Vancouver, BC, Canada

[2] Department of Chemistry and Bioscience, Aalborg University, Aalborg, Denmark

[*] Correspondence:

filip.vanpetegem@gmail.com; +1 604 827 4267

## Key points

- Mutations in the calmodulin protein (CaM) are associated with arrhythmia syndromes.
- This study focuses on understanding the structural characteristics of CaM disease mutants and their interactions with the calcium channel.
- Arrhythmia mutations in CaM can lead to loss of $Ca^{2+}$ binding, uncoupling of $Ca^{2+}$ binding cooperativity, misfolding of the EF-hands, and altered affinity for the calcium channel.
- These results help us to understand how different CaM mutants have distinct effects on structure and interactions with protein targets to cause disease.

This is an Accepted Article that has been peer-reviewed and approved for publication in the The Journal of Physiology, but has yet to undergo copy-editing and proof correction. Please cite this article as an 'Accepted Article'; doi: 10.1113/JP279307.

**ABSTRACT**

Calmodulinopathies are life-threatening arrhythmia syndromes that arise from mutations in calmodulin (CaM), a calcium sensing protein whose sequence is completely conserved across all vertebrates. These mutations have been shown to interfere with the function of cardiac ion channels, including the voltage-gated $Ca^{2+}$ channel $Ca_V1.2$ and the Ryanodine Receptor (RyR2), in a mutation-specific manner. The ability of different CaM disease mutations to discriminate between these channels has been enigmatic. We present crystal structures of several C-terminal lobe mutants and an N-terminal lobe mutant in complex with the $Ca_V1.2$ IQ domain, in conjunction with binding assays and complementary structural biology techniques. One mutation (D130G) causes a pathological conformation, with complete separation of EF-hands within the C-lobe and loss of $Ca^{2+}$ binding in EF-hand 4. Another variant (Q136P) has severely reduced affinity for the IQ domain, and shows changes in the CD spectra under $Ca^{2+}$-saturating conditions when unbound to IQ domain. $Ca^{2+}$ binding to a pair of EF-hands normally proceeds with very high cooperativity, but we find that N98S CaM can adopt different conformations with either one or two $Ca^{2+}$ ions bound to the C-lobe, possibly disrupting the cooperativity. An N-lobe variant (N54I), which causes severe stress-induced arrhythmia, does not show any major changes in complex with the IQ domain, providing a structural basis for why this mutant does not affect function of $Ca_V1.2$. These findings show that different CaM mutants have distinct effects on both the CaM structure and interactions with protein targets, and act via distinct pathological mechanisms to cause disease.

**Keywords:** Calmodulin, calcium channel, structural biology

## INTRODUCTION

Calmodulin (CaM) is a ubiquitously expressed $Ca^{2+}$ sensor and signal transducer that modulates many cellular processes(Friedberg & Rhoads, 2001). It consists of four classical $Ca^{2+}$-binding EF-hands (EF1-4) located in two globular N-terminal (N-lobe) and C-terminal (C-lobe) domains. $Ca^{2+}$ binding to the EF-hands within each lobe is highly cooperative(Beccia *et al.*, 2015), and the different $Ca^{2+}$ affinities between the lobes allow CaM to mediate signaling over a range of cytosolic $Ca^{2+}$ concentrations through interactions with numerous targets, including the L-type voltage-gated $Ca^{2+}$ channel ($Ca_V1.2$)(Ben-Johny & Yue, 2014) and cardiac ryanodine receptor (RyR2)(Van Petegem, 2012; Gong *et al.*, 2019). Upon $Ca^{2+}$ binding, concerted movements of helices in the EF-hands from an antiparallel to orthogonal position allow CaM to undergo a "closed-to-open" structural transition, exposing hydrophobic patches that allow for target recognition. $Ca_V1.2$, the main voltage-gated $Ca^{2+}$ channel isoform expressed in the heart, is known to undergo a $Ca^{2+}$-dependent feedback process, known as $Ca^{2+}$-dependent inactivation (CDI). Binding of CaM to an IQ motif in the C-terminal tail of $Ca_V1.2$ is essential for CDI, and replacement of the consensus isoleucine 1624 residue with alanine was shown to abolish CDI(Peterson *et al.*, 1999; Zuhlke *et al.*, 1999). Additionally, overexpression of $Ca^{2+}$-insensitive CaM drastically prolongs the ventricular action potential in guinea pig ventricular myocytes, giving the first hint that CaM mutations may give a predisposition to ventricular arrhythmias(Alseikhan *et al.*, 2002).

Three human genes (*CALM1*, *CALM2*, and *CALM3*) located on different chromosomes encode for the same CaM protein, and this protein sequence is entirely conserved across vertebrates(Fischer *et al.*, 1988). Despite this redundancy, mutation in only one of the six CaM alleles has been associated with life-threatening cardiac disorders such as long QT syndrome (LQTS) and catecholaminergic polymorphic ventricular tachycardia (CPVT). The first arrhythmogenic CaM mutation was identified in a large Swedish family with severe, dominantly-inherited CPVT, presenting with ventricular arrhythmias, syncope, and sudden cardiac death(Nyegaard *et al.*, 2012). Genome-wide linkage analysis revealed a substitution of asparagine for isoleucine at position 54 of CaM, prompting genetic screening for mutations in *CALM* genes in individuals with CPVT. A *de novo* asparagine to serine substitution at position 98 was subsequently found in a patient with early-onset CPVT. To date, N98S CaM has been identified in eleven families, making it the most prevalent disease-associated CaM

variant(Crotti *et al.*, 2019; Fujita *et al.*, 2019). It is also the mutation with the most phenotypic variability, manifesting as LQTS, CPVT, idiopathic ventricular fibrillation (IVF), or mixed symptoms in different individuals. Another hotspot for CaM variation is position 130, with substitution of aspartate for glycine found in six families(Crotti *et al.*, 2013; Crotti *et al.*, 2019; Wren *et al.*, 2019). D130G CaM gives rise to a strictly LQTS phenotype, in accordance with the observation that most variants in EF4 are associated with LQTS. The Q136P EF4 mutation is one of the few exceptions, identified in a patient diagnosed with mixed LQTS and CPVT symptoms(Makita *et al.*, 2014). The different cardiac phenotypes of different CaM mutations, and even diverse phenotypes of the same mutation, raise questions about the disease mechanism. In particular, the ability of some mutants to associate only with CPVT and not long-QT, or vice versa, has been enigmatic. The N54I mutant, for example, affects the function of RyR2, but spares the CDI of $Ca_V1.2$, but the structural reason for this is unknown.

Here, we structurally characterize four CaM variants by high-resolution X-ray crystallography: an N-lobe mutation (N54I), an EF3 mutation (N98S), and two EF4 mutations (D130G and Q136P). Together with binding assays and NMR data, we shed light on the distinct mechanisms of each CaM disease mutant.

## METHODS

**Cloning, expression, and purification.** The IQ domain of human $Ca_V1.2$ ($Ca_V\alpha_1c77$) (residues 1611-1641) were cloned as previously described(Van Petegem *et al.*, 2005) into a modified pET28 vector containing, in tandem, an N-terminal hexahistidine tag, maltose-binding protein (MBP), and cleavage site for the tobacco etch virus (TEV) protease. Full-length human CaM was cloned into pEGST which lacks any affinity tag. The N54I, N98S, D130G, and Q136P mutations were produced by the QuikChange protocol (Stratagene). Co-expression and co-purification procedures for the CaM:IQ domain complexes were described(Wang *et al.*, 2018).

Samples of WT and D130G $Ca^{2+}$/CaM:IQ complexes were passed through a Superdex 75 10/300 GL (GE Healthcare) gel filtration column for analytical size determination. The protein buffer was exchanged to 25 mM NaCl, 10 mM HEPES, pH 7.4, and 10 mM $CaCl_2$ prior to crystallization.

**TAMRA fluorescence anisotropy experiments.** Buffered solutions, experimental methods, and curve fitting were as previously described(Wang *et al.*, 2018). Differences in the $Ca_V1.2$-IQ peptide affinity between CaM mutants and wild-type were evaluated by a one-way ANOVA at each $Ca^{2+}$-concentration with Dunnett's multiple comparisons test.

**Crystallization, data collection, and structure solution.** Crystals were obtained by hanging-drop vapour diffusion by mixing equal volumes of protein (~25 $mg.ml^{-1}$) and reservoir solution. Complexes of N54I $Ca^{2+}$/CaM:IQ domain were crystallized in a solution of 23.6% PEG 3350 (w/v) and 0.1 M citric acid, pH 4, at 25 $^oC$. Crystals of the N98S $Ca^{2+}$/CaM:IQ domain complex appeared in a solution of 2.1 M DL-malic acid, pH 7.46, at 4 $^oC$. DL-malic acid chelates $Ca^{2+}$ ions; the free $Ca^{2+}$ concentration after mixing the protein buffer (containing 10 mM $CaCl_2$) and reservoir solution was ~10 μM, as measured by an ion-selective electrode (Mettler Toledo perfectION$^{TM}$ combination $Ca^{2+}$). The D130G $Ca^{2+}$/CaM:IQ domain complex crystallized in a solution of 1.86 M ammonium sulfate at 25 $^oC$. The Q136P $Ca^{2+}$/CaM:IQ domain complex appeared in a solution of 15.8% PEG 550 MME (v/v) and 0.1 M sodium acetate, pH 4, at 25 $^oC$.

After flash-freezing in liquid nitrogen, diffraction data were collected at the Stanford Synchrotron Radiation Lightsource beamline 9-2 (N98S and Q136P $Ca^{2+}$/CaM:IQ complexes) and the Advanced Photon Source beamline 23ID-D (N54I and D130G $Ca^{2+}$/CaM:IQ complexes) and processed using XDS(Kabsch, 2010).

The structures were solved by molecular replacement using Phenix(Adams *et al.*, 2010) and using, as search models, F142L $Ca^{2+}$/CaM (PDB ID: 6DAF) for N54I and Q136P $Ca^{2+}$/CaM:IQ, wild-type $Ca^{2+}$/CaM (PDB ID: 2BE6) for N98S $Ca^{2+}$/CaM:IQ, and wild-type $Ca^{2+}$/CaM (PDB ID: 3G43) for D130G $Ca^{2+}$/CaM:IQ. The structures were refined using COOT(Emsley & Cowtan, 2004) and Phenix(Adams *et al.*, 2010). No residues are in disallowed regions of the Ramachandran plot. Final models contain one (Q136P $Ca^{2+}$/CaM:IQ), two (N54I and N98S $Ca^{2+}$/CaM:IQ), or ten (D130G $Ca^{2+}$/CaM:IQ) complexes in the asymmetric unit. A $Na^+$ ion was placed in EF3 of N98S $Ca^{2+}$/CaM (chain A); the electron density and coordination chemistry does not support that for $Ca^{2+}$, $Mg^{2+}$, $Ni^{2+}$, or a water molecule(Zheng *et al.*, 2017). Molecular graphics were prepared using PyMOL (www.pymol.org) (Schrödinger). Statistics for data collection and refinement are shown in

Table 1. Coordinates have been deposited in the Protein Data Bank with accession codes 6U39, 6U3A, 6U3B, and 6U3D.

**Circular dichroism.** Circular dichroism spectra were recorded using a Chirascan-Plus circular dichroism spectrometer for 20 μM CaM in buffer (4 mM HEPES, 20 mM KCl, pH 7.2) with either 1 mM $CaCl_2$ or EDTA added. The spectra were converted to mean residue ellipticity ($\Theta_{MRE}$) after buffer subtraction. Secondary structure elements were calculated using the CDSSTR algorithm(Sreerama & Woody, 2000) with protein reference set 4 on the DichroWeb platform(Whitmore & Wallace, 2004). The algorithm predicts secondary structure elements based on 6 classifications: regular and distorted α-helix, regular and distorted ß-sheet, turns, and unordered. Statistically significant differences ($P < 0.05$) in structural elements between CaM variants were evaluated by a two-way ANOVA with a Holm-Sidak *post hoc* test.

**NMR experiments.** $^{15}$N-labelled WT/D96V/N98S CaM was expressed and purified as previously described(Wang *et al.*, 2018). 200 μM of $Ca^{2+}$-bound WT/D96V/N98S CaM was saturated with a synthetic peptide (>97% purity, Proteogenix, France) corresponding to the IQ domain of human $Ca_V1.2$ (DEVTVGKFYATFLIQEYFRKFKKRKEQGLVGKPS-$NH_2$). The sample was then centrifuged for 1 min at 12,300 x g and the supernatant was loaded onto a Superdex 75 HiLoad 16/60 gel filtration column equilibrated with 2 mM HEPES, 10 mM KCl, 1 mM $CaCl_2$, pH 6.7. The eluate was concentrated to 500 μL in a 3 kDa MWCO filter. All NMR samples contained: 200 μM $Ca^{2+}$CaM:IQ complex, 2 mM HEPES, 10 mM KCl, 1 mM $CaCl_2$, 2 mM $NaN_3$, 0.1 mM TSP-$d_4$ (sodium 2,2,3,3-tetradeutero, 3-(trimethylsilyl) propionate) dissolved in 95 % $H_2O$, 5 % $D_2O$. WT and N98S samples had pH 6.58, while the D96V sample had pH 6.52.

$^{1}$H-$^{15}$N-HSQC NMR spectra were recorded on a BRUKER AVIII-600 MHz spectrometer equipped with a CPP-TCI probe. Spectra were acquired at 298.1 K. BRUKER TopSpin 3.5pl6 was used for recording and processing.

**RESULTS**

In this manuscript, we use the numbering based on the open reading frame of CaM, with the initiating methionine denoted as residue 1.

**Calmodulin mutants have different effects on binding to the $Ca_V1.2$ IQ domain**

We investigated several CaM disease mutants previously associated with only CPVT, only LQTS, or mixed LQTS/CPVT phenotypes. To investigate whether they have aberrant interactions with the $Ca_V1.2$ IQ domain, we used fluorescence anisotropy (FA) to measure binding affinity of full-length CaM for the IQ domain over a range of $Ca^{2+}$ concentrations (data represent mean ± standard deviation of 3 replicates) (Fig. 1).

N54I CaM binds the IQ domain with affinities comparable to wild-type (WT) CaM at all tested $Ca^{2+}$ concentrations. Because the C-lobe is responsible for high-affinity tethering of CaM to the $Ca_V1.2$ IQ domain, it is unsurprising that a mutation in the N-lobe has little effect on the affinity of full-length CaM for the IQ domain(Fallon *et al.*, 2005; Van Petegem *et al.*, 2005). Additionally, this mutation was previously shown to have no effect on $Ca_V1.2$ CDI(Limpitikul *et al.*, 2014; Yin *et al.*, 2014). As described before(Wang *et al.*, 2018), N98S CaM displays a modest but statistically significant reduction in affinity for the IQ domain in the range of 100 nM - 10 μM $Ca^{2+}$. The largest effect is seen for D130G and Q136P CaM, which have decreased affinities at all $Ca^{2+}$ concentrations; in particular, the mutants have 10- to 1000-fold weaker affinity for the IQ domain at 100 nM - 10 μM $Ca^{2+}$, with the Q136P mutation having the most severe impairment in binding. Compared to EF3 CaM mutations, it appears that mutations in EF4 are more detrimental to CaM binding to the $Ca_V1.2$ IQ domain(Wang *et al.*, 2018).

Previously, the N54I and N98S CaM were analyzed via circular dichroism (CD), showing only very subtle differences from WT CaM (1-2%)(Sondergaard *et al.*, 2015a). Here we analyzed the Q136P and D130G mutants via CD (data represent mean ± standard deviation of 4 replicates) (Fig 1B-D). Both of these showed significant differences in $Ca^{2+}$-saturated conditions, but not under $Ca^{2+}$-free conditions. These two mutants thus have the largest effects on both binding to the IQ domain, and $Ca^{2+}$-saturated structure. To gain more insights into these mutations, we proceeded with solving crystal structures.

**Crystal structure of the D130G $Ca^{2+}$/CaM:IQ complex**

Asp130 coordinates a $Ca^{2+}$ ion in EF4. The D130G CaM mutation has been associated with LQTS(Crotti *et al.*, 2013; Reed *et al.*, 2015; Boczek *et al.*, 2016) and appears to be a CaM mutation hotspot(Crotti *et al.*, 2019). Given the reduced affinity for the IQ domain in a range

of $Ca^{2+}$ concentrations, we sought to structurally characterize the D130G $Ca^{2+}$/CaM:IQ domain interaction and solved a 2.4Å crystal structure of the complex in 10mM $CaCl_2$.

There are ten complexes in the asymmetric unit (AU), and despite the high $Ca^{2+}$ concentration (mM) used during crystallization, the $Ca^{2+}$-coordinating pocket of EF4 is completely disrupted with large changes in main chain positions and loss of $Ca^{2+}$ binding (Fig. 2A-C, Supp video 1). The absence of $Ca^{2+}$ has numerous consequences. Electron density for many of the $Ca^{2+}$-coordinating side chains in EF4 is absent due to increased flexibilities. Asp132 and Asp134, whose side chains protrude into the binding pocket to coordinate $Ca^{2+}$ in the wild-type structure, rotate and project outwards from the pocket in the mutant. Glu141 also relaxes to a different position, shifting away from the loop by ~3 Å. Glycine has more conformational flexibility than other residues and has the largest allowable area in the Ramachandran plot. Due to this increased flexibility, the D130G EF4 relaxes to a wider conformation than in WT $Ca^{2+}$/CaM. Widths of the EF4 loop between different D130G $Ca^{2+}$/CaM chains are also variable when comparing different complexes in the asymmetric unit; for example, EF4 of chain K is wider than chain M, which is narrower and more elongated. The D130G EF4 conformation is also different from that of WT apoCaM, which retains a tight loop structure despite the lack of bound ions (Fig. 2D). Thus, the conformation of EF4 in D130G resembles neither a WT $Ca^{2+}$/CaM nor WT apoCaM EF-hand and adopts an intrinsic flexibility.

This local change in EF4 has dramatic consequences on the overall conformation, resulting in an unwinding of the D130G C-lobe, with EF-hands 3 and 4 physically uncoupled (Fig. 2E). Helices E and F align reasonably to wild-type, but the loop between helices F-G in wild-type becomes α-helical in the D130G mutant, such that helices F-G form a single, continuous α helix. In the crystal structure, this helix is involved in packing interactions with a neighboring D130G CaM:IQ complex, giving rise to an apparent dimer (Fig. 3A-B). In fact, all ten complexes in the AU assemble into five of such dimers, suggesting it is relatively stable. However, size exclusion chromatography shows that the wild-type and D130G $Ca^{2+}$/CaM:IQ complexes elute at volumes corresponding to a single complex (Fig. 3C), and the dimerization may thus only arise at high concentrations as found within crystals.

As a result of the C-lobe misfolding, interactions with the IQ domain residues are different. In WT $Ca^{2+}$/CaM, both the N-lobe and C-lobe wrap around the IQ domain to form a compact,

globular structure(Fallon *et al.*, 2005; Van Petegem *et al.*, 2005) (Fig. 4A). There are binding grooves in the N-lobe for the IQ domain aromatic anchors Phe1618, Tyr1619, and Phe1622, and the C-lobe forms hydrophobic pockets for the IQ domain anchoring residues Ile1624, Tyr1627, and Phe1628. The D130G N-lobe displays small rearrangements around the IQ domain compared to wild-type (Fig. 4B). However, there is inherent variability in the positioning of the N-lobe as the WT N-lobe is able to adopt a number of different orientations around the IQ domain(Van Petegem *et al.*, 2005), so this change is likely not significant. Due to the misfolding of the D130G C-lobe, the contacts between this lobe and the IQ domain are completely different, as helices G and H no longer embrace the IQ domain (Fig. 4C-D). Ile1624 represents the "I" in IQ domain and is critical for CDI(Peterson *et al.*, 1999; Zuhlke *et al.*, 1999). In WT CaM, Ile1624 is bound in a hydrophobic pocket of the C-lobe. In the D130G mutant, however, C-lobe residues form few contacts with Ile1624. Tyr1627, the primary C-terminal aromatic anchor which is buried in a methionine-rich pocket in WT CaM, is largely solvent-exposed in the mutant complex, along with the second major anchoring residue Phe1628. This is functionally significant because the WT C-lobe acts as an anchor to tether CaM to the IQ domain and the WT N-lobe is labile and can adopt a variety of positions(Van Petegem *et al.*, 2005). However, in the D130G mutant, the N-lobe forms the majority of contacts with the IQ domain while the C-lobe offers few interactions.

The D130G mutation thus has several effects on CaM and its interactions with the $Ca_V1.2$ IQ domain: loss of $Ca^{2+}$ binding in EF4, misfolding of the C-lobe that physically uncouples EF3 and EF4, and disrupted interactions with the IQ domain. All of these factors may contribute to loss of $Ca_V1.2$ CDI and the accompanying LQTS phenotype observed in disease.

**Crystal structure of the Q136P $Ca^{2+}$/CaM:IQ complex**

Gln136 is also located in the $Ca^{2+}$-coordinating loop of EF4, although the glutamine side chain does not directly participate in $Ca^{2+}$ binding. The Q136P mutation was identified in a girl who exhibited both LQTS and CPVT phenotypes(Makita *et al.*, 2014). Given the severe perturbations in binding affinity for the IQ domain, we wondered whether this CaM mutation also results in large conformational distortions like the D130G mutation. We solved a 1.7Å crystal structure of Q136P $Ca^{2+}$/CaM:IQ domain complex, obtained with 10mM $CaCl_2$. This structure contains one complex in the AU.

Despite the strict Ramachandran constraints imposed by mutation to proline, Q136P CaM is still able to bind $Ca^{2+}$ in EF4, at least under saturating $Ca^{2+}$ conditions. Coordination distances between the $Ca^{2+}$ ion and residues in the EF4 loop are comparable to WT CaM (2.3-2.6 Å) (Fig. 5A, Supp video 2). The carbonyl oxygen between Gly135 and Pro136 has shifted by 1.9 Å (Fig. 5B), resulting in a less favourable backbone conformation which may result in a lowered $Ca^{2+}$ affinity, as suggested before for this mutant(Makita *et al.*, 2014). Tyr100, located in the EF3 loop, has reoriented, making packing interactions with Pro136 (Fig. 5C). This position is not possible in WT as it would clash with Gln136. As a result, there is a shift in the position of the EF3 loop residues relative to the EF4 loop. In addition, changes in the C-lobe alter interactions with the bound IQ domain (Fig. 5D,E). There are small changes in side chain positions of the IQ domain, particularly Tyr1627and Phe1628, as well as altered electrostatics of the Q136P C-lobe binding surface.

**Crystal structure of N98S $Ca^{2+}$/CaM in complex with the IQ domain**

N98S CaM has been identified individually in patients presenting with CPVT, LQTS, IVF, and SUD phenotypes and is the most prevalent out of all CaM disease mutations(Nyegaard *et al.*, 2012; Makita *et al.*, 2014; Crotti *et al.*, 2019). The different phenotypes suggest it can affect the function of multiple targets. In WT CaM, Asn98 coordinates a $Ca^{2+}$ ion in EF3 of the C-lobe. A previously determined structure of the N98S mutant showed minimal effects on structure(Wang *et al.*, 2018), a result that seems at odds with the fact that this mutation can slow down CDI significantly, and has lowered affinity for the IQ domain in the concentration range of 100 nM – 10 μM free $Ca^{2+}$ (Limpitikul *et al.*, 2014; Wang *et al.*, 2018) (Fig 1). However, the previous structure was obtained in the absence of any target peptide. Here we were able to solve a structure in complex with the $Ca_V1.2$ IQ domain. Fortuitously, the crystals were obtained at a free $Ca^{2+}$ concentration of ~10 μM (see Methods), a more physiologically relevant $Ca^{2+}$ concentration.

We solved the corresponding structure at 1.65 Å resolution. There are two complexes in the asymmetric unit, and surprisingly, N98S CaM adopts different conformations in these two complexes (Supp video 3). In one complex (chains B and D), the N98S $Ca^{2+}$/CaM:IQ complex resembles the wild-type structure (Fig. 6). A $Ca^{2+}$ ion is bound in EF3, with coordination contributed by both Asn98 and Ser98 side chains (Fig. 6A-B). The N98S C-lobe superposes well with the WT C-lobe structure (RMSD 0.469 Å) (Fig. 6C) and positioning of

the N98S C-lobe around the IQ domain is similar to wild-type (Fig. 6D). Small changes can be seen in the orientation of the N98S N-lobe relative to the IQ domain, but this lobe was previously reported to adopt multiple conformations(Van Petegem *et al.*, 2005), and this change is unlikely to be a result of the mutation.

The second N98S $Ca^{2+}$/CaM:IQ complex (chains A and C) in the asymmetric unit does not have a $Ca^{2+}$ ion bound in EF3. Glu105, which coordinates the $Ca^{2+}$ in WT CaM, relaxes away from the $Ca^{2+}$ binding pocket due to lack of stabilizing $Ca^{2+}$-coordination interactions, leading to large-scale allosteric changes and distortions in the C-lobe (Fig. 7A-B). Interestingly, a $Na^{+}$ ion is bound in lieu of the $Ca^{2+}$ ion (see Methods). This $Na^{+}$ ion is coordinated by the side chains of Asp94, Asp96, Ser98, the carbonyl oxygen of Tyr100, and a water molecule. The overall conformation of the C-lobe is reminiscent of the N98I and D96V mutants(Wang *et al.*, 2018). In these cases, $Ca^{2+}$ binding to EF3 was abolished, despite the presence of saturating (10 mM) $Ca^{2+}$ levels. However, the precise conformation of side chains in the EF3 loop is different (Fig. 8A). For example, Tyr100 forms stacking interactions with Ile98 and Gln136 in the N98I mutant, but for the N98S mutant Tyr100 takes on a position similar to WT.

Although the conformations of side chains in EF3 are different between the N98S, D96V, and N98I mutants, the overall structures of the C-lobes are highly comparable, all of which are distinct from the WT $Ca^{2+}$/C-lobe and WT apoC-lobe (Fig. 8B). Additionally, N98S CaM displays the same reorientation of N- and C-lobes around the IQ domain that was observed for the N98I and D96V mutants, altering its interactions with the IQ domain compared to wild-type (Fig. 8C).

The binding of $Ca^{2+}$ to a pair of EF hands in WT CaM has been found to proceed with a very high degree of cooperativity(Minowa & Yagi, 1984; Tsalkova & Privalov, 1985; Wang, 1985; Linse *et al.*, 1991; Ikura, 1996; Sorensen & Shea, 1998; Masino *et al.*, 2000; VanScyoc & Shea, 2001; Beccia *et al.*, 2015), such that it is rare to have a stable version with only one $Ca^{2+}$ bound to an individual lobe. However, the N98S mutation may be able to reduce this cooperativity, yielding a C-lobe with only a single $Ca^{2+}$ bound at a physiologically relevant $Ca^{2+}$ concentration. This is in contrast with our previous analysis of this mutant in the absence of the IQ domain, whereby four molecules in the asymmetric unit all retained $Ca^{2+}$ binding(Wang *et al.*, 2018). The likely explanation for this discrepancy is the amount of free

$Ca^{2+}$ in the crystallization condition (μM in this study, mM in the previous study). However, as another difference is the presence or absence of an IQ domain, we wished to test the effect of the mutant, in the presence of IQ domain, under saturating $Ca^{2+}$ levels.

**Investigation of the N98S $Ca^{2+}$/CaM:IQ complex via NMR spectroscopy**

As we were unable to crystallize the N98S CaM:IQ complex under mM free $Ca^{2+}$ concentrations, we instead reverted to NMR spectroscopy, and measured HSQC spectra under saturating $Ca^{2+}$ concentration (Fig. 9). Overlay of the [$^{1}$H-$^{15}$N]-HSQC spectra of N98S and WT $Ca^{2+}$/CaM:IQ complexes shows that the N98S mutant is highly comparable to the wild-type population with only minor changes that can be expected as a consequence of a single point mutation. The differences between wild-type and N98S CaM are much smaller than the differences seen between the wild-type and D96V (Fig. 10).

These results thus suggest that the difference in conformations for N98S CaM, observed previously(Wang *et al.*, 2018) and in this study, are due to the free $Ca^{2+}$ concentrations, and not to the presence or absence of the IQ domain.

**Crystal structure of the N54I $Ca^{2+}$/CaM:IQ complex**

While the previous structures have focused on CaM mutations associated with LQTS, the most prevalent phenotype for CaM variants, we wished to compare it to the structure of a CaM mutant not associated with LQTS. The N54I mutation was initially identified in a large Swedish family with severe CPVT and subsequently found in an individual with IVF(Nyegaard *et al.*, 2012; Crotti *et al.*, 2019). We crystallized N54I $Ca^{2+}$/CaM in a complex with the IQ domain at 10mM $CaCl_2$ and solved the structure at 1.75 Å resolution.

Unlike many of the C-lobe mutants which affect residues in EF-hand loops, the N54I mutation is located in helix C of the N-lobe. The overall structure is similar to WT $Ca^{2+}$/CaM, with N54I CaM binding to the IQ domain in a parallel orientation and full $Ca^{2+}$ occupancy in all four EF-hands (Fig. 11A). The N54I N-lobe aligns well with WT N-lobe (RMSD 0.361 Å) (Fig. 11B). The largest change is immediately adjacent to the mutation site, with a change in the side chain conformation of Gln50 (Fig. 11C). However, no changes are detected in residues that coordinate $Ca^{2+}$, and no significant overall conformational changes are observed.

These results support the lack of any significant effect of the N54I mutation on CDI of $Ca_V1.2$(Limpitikul *et al.*, 2014; Yin *et al.*, 2014), and because of the CPVT phenotype in several patients, suggest that any mechanism of disease is likely to involve RyR2 or other ion channels instead(Pancaroglu & Van Petegem, 2018; Saljic *et al.*, 2019).

**DISCUSSION**

Calmodulinopathies include a range of dominantly inherited arrhythmogenic syndromes such as LQTS, CPVT, IVF, and atypical/mixed phenotypes(Nyegaard *et al.*, 2012; Crotti *et al.*, 2013; Marsman *et al.*, 2014; Crotti *et al.*, 2019). These life-threatening disorders are often *de novo* and early-onset and can be caused by mutation in any one of the three *CALM* genes. In the heart, CaM modulates voltage-gated calcium, sodium, and potassium channels, as well as RyR2(Van Petegem *et al.*, 2012; Sorensen *et al.*, 2013; Lau *et al.*, 2014; Sun & MacKinnon, 2017). $Ca_V1.2$ contributes towards depolarization, and CaM-mediated CDI of the channel is essential for proper repolarization. Several LQTS-associated CaM mutants were found to have decreased $Ca^{2+}$ affinity and reduced CDI of $Ca_V1.2$, thus resulting in a lengthened action potential and QT interval prolongation(Limpitikul *et al.*, 2014; Yin *et al.*, 2014).

Here we analyze the effect of mutations on the structure of CaM in the presence of the $Ca_V1.2$ IQ domain. An intrinsic limitation is that we are lacking the upstream EF-hand domain, which also plays a role in CDI(Ben Johny *et al.*, 2013). So far any $Ca_V$ construct containing this element has failed to produce properly folded protein, in contrast to the progress made for voltage-gated sodium channels(Wang *et al.*, 2012; Gabelli *et al.*, 2014; Wang *et al.*, 2014; Gardill *et al.*, 2019; Yoder *et al.*, 2019). Our structural studies of CaM disease mutants show that different mutations have distinct effects on the structure in the presence of the $Ca_V1.2$ IQ domain, despite the fact that most, but not all, have a similar functional outcome on CDI:

1) Permanent loss of $Ca^{2+}$ binding to EF3, resulting in a distorted C-lobe. EF3 and EF4 are still in physical contact (D96V and N98I mutants)(Wang *et al.*, 2018).

2) Decreased affinity of EF3 for $Ca^{2+}$, leading to potential loss of cooperativity of $Ca^{2+}$ binding to EF3 and EF4. At high mM $Ca^{2+}$ concentrations, both EF3 and EF4 are $Ca^{2+}$ occupied(Wang *et al.*, 2018). At lower, μM $Ca^{2+}$ concentrations, EF3 can be $Ca^{2+}$ free, and EF4 $Ca^{2+}$ occupied, leading to a distorted C-lobe conformation (N98S).

3) Abolished binding of $Ca^{2+}$ to EF4 and a structural distortion that physically uncouples EF3 and EF4 (D130G).

4) Structural distortions of $Ca^{2+}$/CaM that appear only visible in the absence of an IQ domain. The presence of an IQ domain stabilizes the structure (Q136P).

5) Minimal effect on $Ca^{2+}$/CaM, but structural distortions of the $Ca^{2+}$-free state, which increase the affinity for the IQ domain (F142L)(Wang *et al.*, 2018).

6) No significant effects on the structure, at least in complex with the IQ domain (N54I).

Of note, all LQTS-associated CaM mutants investigated so far still maintain substantial affinity for the IQ domain under low $Ca^{2+}$-conditions, making the mutant versions effective competitors for wild-type CaM. As apoCaM pre-association with the IQ domain is essential for CDI, this immediately explains the dominant nature of the calmodulinopathies: it implies that the fraction of the channels preassociated with a LQTS-mutant CaM will simply not undergo CDI due to the perturbations of the $Ca^{2+}$-bound state or alterations in the $Ca^{2+}$ affinity and cooperativity. The resulting loss of CDI for this fraction of channels is sufficient to cause LQTS(Limpitikul *et al.*, 2014).

The most dramatic effects are observed for the D130G mutant. Due to misfolding of the C-lobe, the D130G $Ca^{2+}$/C-lobe no longer forms significant contacts with the IQ domain, and it is the D130G $Ca^{2+}$/N-lobe that makes the majority of interactions with the IQ domain (Fig. 4). This is also reflected in the decreased affinity of D130G CaM for the IQ domain, compared to wild-type, across all $Ca^{2+}$ concentrations tested (Fig. 1). Helices F-G form a continuous α helix in the D130G crystal structure (Fig. 3), and the protein forms a dimer in all ten molecules of the AU. The D130G $Ca^{2+}$/CaM:IQ complex was found to be in a 1:1 complex in solution, so this dimer may not exist in physiological conditions. Because C-lobe binding to the $Ca_V1.2$ IQ domain is critical for CDI(Peterson *et al.*, 1999; Zuhlke *et al.*, 1999), the grossly perturbed D130G $Ca^{2+}$/C-lobe:IQ domain interaction would explain the strong suppression of CDI(Limpitikul *et al.*, 2014).

The D130G mutation also disrupts the $Ca^{2+}$-coordination pocket of EF4 and abolishes ion binding. Indeed, the D130G mutation has 54-fold lower affinity compared to wild-type(Crotti *et al.*, 2013). It is thus possible that similar uncoupling of EF3 and EF4 also occurs in the absence of the IQ domain, but this remains to be tested. Although we don't have a high-

resolution structure of this mutant in the absence of $Ca^{2+}$, the CD data suggest that there are no major distortions in the $Ca^{2+}$-free state (Fig. 1B). Given the severe C-lobe conformational distortions (Fig. 2E), changes in surface electrostatics (Fig. 4) and reduced $Ca^{2+}$ affinity, it is likely that D130G CaM interactions with other binding targets are also affected, not just that with the $Ca_V1.2$ IQ domain. Indeed, out of six arrhythmia-causing CaM variants (N54I, F90L, D96V, N98S, D130G, and F142L) studied by Berchtold *et al.*, the D130G mutant has the most profound effect on viability of a vertebrate cell line, suggesting that D130G CaM, in the absence of any WT CaM, is unable to support basic cell functions(Berchtold *et al.*, 2016). D130G CaM was shown to increase SR $Ca^{2+}$ release from RyR2 and lowered both the activation and termination threshold for store overload-induced $Ca^{2+}$ release (SOICR)(Sondergaard *et al.*, 2015b). It was also found to increase the fetal $Na_V1.5$ late current in heterologous cells (but not in fetal ventricular myocytes) and to diminish both CaMKII activation and CaMKII substrate phosphorylation(Yin *et al.*, 2014; Berchtold *et al.*, 2016). In addition to direct regulation by CaM, cardiac ion channels are also regulated by CaMKII phosphorylation, so the D130G CaM mutation has possible combined effects of aberrant direct modulation of targets as well as aberrant indirect regulation via CaMKII. The large number of targets affected by D130G CaM aligns with the observation that this mutant causes a severe, early-onset disease phenotype with numerous probands diagnosed at birth(Boczek *et al.*, 2016).

Given the severe reduction in affinity for the IQ domain (Fig. 1), it was surprising that the Q136P $Ca^{2+}$/CaM:IQ complex displays subtle conformational changes compared to WT $Ca^{2+}$/CaM:IQ in the crystal structure (Fig. 5). It is likely that the IQ domain helps to stabilize the structure of Q136P $Ca^{2+}$/CaM to more closely resemble the wild-type conformation. The Q136P variant, when unbound to the $Ca_V1.2$ IQ domain, may adopt a pathological conformation that affects interactions with other molecular targets. Because the Q136P mutant is also associated with CPVT(Makita *et al.*, 2014), it is likely to result in dysregulation of RyR2. Indeed, this mutant was found to decrease both the activation and termination threshold for SOICR, increasing the fractional ER $Ca^{2+}$ release(Sondergaard *et al.*, 2019). Further biophysical characterization of Q136P CaM on the function of various ion channels is necessary to understand its range of disease pathology.

A well-known feature of CaM is high cooperativity of $Ca^{2+}$ binding within its individual lobes. In the past, there has been some contention about the extent of $Ca^{2+}$ binding

cooperativity. It is generally accepted that a high level of positive cooperativity exists between EF1 and EF2 in the lower affinity N-lobe, and EF3 and EF4 in the higher affinity C-lobe(Minowa & Yagi, 1984; Tsalkova & Privalov, 1985; Wang, 1985; Linse *et al.*, 1991; Ikura, 1996; Sorensen & Shea, 1998; Masino *et al.*, 2000; VanScyoc & Shea, 2001; Beccia *et al.*, 2015). Our crystal structure of the N98S $Ca^{2+}$/CaM:IQ domain is distinctive because it shows uncoupled $Ca^{2+}$-binding cooperativity in the C-lobe, where a $Ca^{2+}$ ion occupies EF4 but is absent in EF3 (Fig. 7). This is observed for one complex in the AU, whereas the other complex retains $Ca^{2+}$ ions at all four sites (Fig. 6). This suggests that there would be an effect on the Hill coefficient, but we were unable to test this via intrinsic CaM fluorescence, because the IQ peptide interferes with the Tyr fluorescence of CaM.

The situation is different for the D96V and N98I mutations, where $Ca^{2+}$ binding to EF3 seems permanently disrupted(Wang *et al.*, 2018). The current structure also highlights the importance of free $Ca^{2+}$ concentration, as a previous structure of the N98S variant at high $Ca^{2+}$ concentration exhibited only the fully $Ca^{2+}$-saturated CaM conformation(Wang *et al.*, 2018). Our structure gives new insights into the disease mechanism of N98S. In the 4 $Ca^{2+}$-bound state, N98S CaM exhibits strain in the main chain of EF3. In the 3 $Ca^{2+}$-bound state, N98S CaM undergoes large conformational changes in the C-lobe that alter interactions with the $Ca_V1.2$ IQ domain in a manner similar to the previously characterized D96V and N98I mutants(Wang *et al.*, 2018), consistent with the observation that N98S CaM is able to mildly suppress $Ca_V1.2$ CDI(Limpitikul *et al.*, 2014). N98S CaM has also been shown to dysregulate RyR2(Nyegaard *et al.*, 2012; Sondergaard *et al.*, 2015a; Sondergaard *et al.*, 2015b). In addition, a cryo-EM structure of the KCNQ1 channel in complex with $Ca^{2+}$/CaM showed a direct interaction between Asn98 and the voltage-sensing domain(Sun & MacKinnon, 2017), and introducing the N98S mutation resulted in a right shift of the conductance-voltage (G-V) relationship. Depending on which interactions with various protein targets are affected, several pathological outcomes are possible. This may explain why the N98S variant results in a broad range of disease phenotypes, including CPVT, LQTS, IVF, and SUD phenotypes in different individuals(Nyegaard *et al.*, 2012; Makita *et al.*, 2014; Crotti *et al.*, 2019).

The majority (80%) of CaM variants are located in the C-lobe, with 89% of these affecting $Ca^{2+}$-binding residues. To date, only two human disease mutations have been identified in the N-lobe of CaM, one of which is the CPVT-associated N54I variant in helix C(Nyegaard *et al.*, 2012; Crotti *et al.*, 2019). This mutation does not affect $Ca_V1.2$ CDI(Limpitikul *et al.*,

2014; Yin *et al.*, 2014). Indeed, we found N54I CaM to have little effect on interactions with the $Ca_V1.2$ IQ domain, both in terms of binding affinities (Fig. 1A) and structure (Fig. 11). Even by itself, N54I CaM displays similar secondary structural elements to WT CaM(Sondergaard *et al.*, 2015a). The mutation does not alter the C-lobe $Ca^{2+}$ affinity, and only minutely impacts the N-lobe $Ca^{2+}$ affinity(Nyegaard *et al.*, 2012; Sondergaard *et al.*, 2015a; Sondergaard *et al.*, 2015b). However, since the N-lobe has also been shown to associate with a CaM binding region, previously termed NSCaTE, near the N-terminus of the channel(Dick *et al.*, 2008; Liu & Vogel, 2012), one possibility remains that the mutation affects this interaction. Due to the linkage of N54I CaM to CPVT(Nyegaard *et al.*, 2012), it is likely that the major molecular pathological mechanism involves RyR2. N54I CaM did not show compromised interactions with a peptide of the RyR2 calmodulin binding domain (CaMBD2) at low or high $Ca^{2+}$ concentrations(Nyegaard *et al.*, 2012), so this variant is able to compete with WT CaM for binding to RyR2. N54I CaM displayed increased RyR2 open probability, RyR2-mediated $Ca^{2+}$ release, and susceptibility for SOICR(Hwang *et al.*, 2014; Sondergaard *et al.*, 2015b). Zebrafish embryos injected with N54I CaM mRNA displayed increased heart rate under β-adrenergic stimulation, analogous to adrenergic induced tachycardia in humans(Sondergaard *et al.*, 2015a). Given the lack of structural and functional effects of N54I CaM on $Ca_V1.2$, aberrant regulation of RyR2 is the more probable cause of CPVT. Of note, a recent report also found an effect of the N54I mutation on the $Ca^{2+}$-activated potassium channel SK3, showing an additional ion channel to play a role in the pathophysiology of CaM arrhythmia mutations(Saljic *et al.*, 2019).

Thus far, all structural studies of CaM disease mutations have been performed in the context of the $Ca_V1.2$ IQ domain. However, with available cryo-EM structures of CaM bound to full-length RyR2(Gong *et al.*, 2019) or KCNQ1 potassium channels(Sun & MacKinnon, 2017), as well as NMR and crystal structures of $Na_V1.5$ cytosolic fragments bound to apoCaM(Chagot & Chazin, 2011; Wang *et al.*, 2012; Gabelli *et al.*, 2014; Wang *et al.*, 2014) or $Ca^{2+}$/CaM(Sarhan *et al.*, 2012; Johnson *et al.*, 2018; Gardill *et al.*, 2019), a structural investigation of arrhythmogenic CaM variants to other cardiac ion channels should be possible.

**REFERENCES**

Adams PD, Afonine PV, Bunkoczi G, Chen VB, Davis IW, Echols N, Headd JJ, Hung LW, Kapral GJ, Grosse-Kunstleve RW, McCoy AJ, Moriarty NW, Oeffner R, Read RJ, Richardson DC, Richardson JS, Terwilliger TC & Zwart PH (2010). PHENIX: a comprehensive Python-based system for macromolecular structure solution. *Acta Crystallogr D Biol Crystallogr* **66,** 213-221.

Alseikhan BA, DeMaria CD, Colecraft HM & Yue DT (2002). Engineered calmodulins reveal the unexpected eminence of Ca2+ channel inactivation in controlling heart excitation. *Proc Natl Acad Sci U S A* **99,** 17185-17190.

Beccia MR, Sauge-Merle S, Lemaire D, Bremond N, Pardoux R, Blangy S, Guilbaud P & Berthomieu C (2015). Thermodynamics of Calcium binding to the Calmodulin N-terminal domain to evaluate site-specific affinity constants and cooperativity. *J Biol Inorg Chem* **20,** 905-919.

Ben-Johny M & Yue DT (2014). Calmodulin regulation (calmodulation) of voltage-gated calcium channels. *J Gen Physiol* **143,** 679-692.

Ben Johny M, Yang PS, Bazzazi H & Yue DT (2013). Dynamic switching of calmodulin interactions underlies Ca2+ regulation of CaV1.3 channels. *Nat Commun* **4,** 1717.

Berchtold MW, Zacharias T, Kulej K, Wang K, Torggler R, Jespersen T, Chen JN, Larsen MR & la Cour JM (2016). The Arrhythmogenic Calmodulin Mutation D129G Dysregulates Cell Growth, Calmodulin-dependent Kinase II Activity, and Cardiac Function in Zebrafish. *J Biol Chem* **291,** 26636-26646.

Boczek NJ, Gomez-Hurtado N, Ye D, Calvert ML, Tester DJ, Kryshtal D, Hwang HS, Johnson CN, Chazin WJ, Loporcaro CG, Shah M, Papez AL, Lau YR, Kanter R, Knollmann BC & Ackerman MJ (2016). Spectrum and Prevalence of CALM1-, CALM2-, and CALM3-Encoded Calmodulin Variants in Long QT Syndrome and Functional Characterization of a Novel Long QT Syndrome-Associated Calmodulin Missense Variant, E141G. *Circ Cardiovasc Genet* **9,** 136-146.

Chagot B & Chazin WJ (2011). Solution NMR structure of Apo-calmodulin in complex with the IQ motif of human cardiac sodium channel NaV1.5. *J Mol Biol* **406,** 106-119.

Crotti L, Johnson CN, Graf E, De Ferrari GM, Cuneo BF, Ovadia M, Papagiannis J, Feldkamp MD, Rathi SG, Kunic JD, Pedrazzini M, Wieland T, Lichtner P, Beckmann BM, Clark T, Shaffer C, Benson DW, Kaab S, Meitinger T, Strom TM, Chazin WJ, Schwartz PJ & George AL, Jr (2013). Calmodulin mutations associated with recurrent cardiac arrest in infants. *Circulation* **127,** 1009-1017.

Crotti L, Spazzolini C, Tester DJ, Ghidoni A, Baruteau AE, Beckmann BM, Behr ER, Bennett JS, Bezzina CR, Bhuiyan ZA, Celiker A, Cerrone M, Dagradi F, De Ferrari GM, Etheridge SP, Fatah M, Garcia-Pavia P, Al-Ghamdi S, Hamilton RM, Al-Hassnan ZN, Horie M, Jimenez-Jaimez J, Kanter RJ, Kaski JP, Kotta MC, Lahrouchi N, Makita N, Norrish G, Odland HH, Ohno S, Papagiannis J, Parati G, Sekarski N, Tveten K, Vatta M, Webster G, Wilde AAM, Wojciak J, George AL, Ackerman MJ & Schwartz PJ (2019). Calmodulin mutations and life-threatening cardiac arrhythmias: insights from the International Calmodulinopathy Registry. *Eur Heart J*.

Dick IE, Tadross MR, Liang H, Tay LH, Yang W & Yue DT (2008). A modular switch for spatial Ca2+ selectivity in the calmodulin regulation of CaV channels. *Nature* **451,** 830-834.

Emsley P & Cowtan K (2004). Coot: model-building tools for molecular graphics. *Acta Crystallogr D Biol Crystallogr* **60,** 2126-2132.

Fallon JL, Halling DB, Hamilton SL & Quiocho FA (2005). Structure of calmodulin bound to the hydrophobic IQ domain of the cardiac Ca(v)1.2 calcium channel. *Structure* **13,** 1881-1886.

Fischer R, Koller M, Flura M, Mathews S, Strehler-Page MA, Krebs J, Penniston JT, Carafoli E & Strehler EE (1988). Multiple divergent mRNAs code for a single human calmodulin. *J Biol Chem* **263,** 17055-17062.

Friedberg F & Rhoads AR (2001). Evolutionary aspects of calmodulin. *IUBMB Life* **51,** 215-221.

Fujita S, Nakagawa R, Futatani T, Igarashi N, Fuchigami T, Saito S, Ohno S, Horie M & Hatasaki K (2019). Long QT syndrome with a de novo CALM2 mutation in a 4-year-old boy. *Pediatr Int*.

Gabelli SB, Boto A, Kuhns VH, Bianchet MA, Farinelli F, Aripirala S, Yoder J, Jakoncic J, Tomaselli GF & Amzel LM (2014). Regulation of the NaV1.5 cytoplasmic domain by calmodulin. *Nat Commun* **5,** 5126.

Gardill BR, Rivera-Acevedo RE, Tung CC & Van Petegem F (2019). Crystal structures of Ca(2+)-calmodulin bound to NaV C-terminal regions suggest role for EF-hand domain in binding and inactivation. *Proc Natl Acad Sci U S A*.

Gong D, Chi X, Wei J, Zhou G, Huang G, Zhang L, Wang R, Lei J, Chen SRW & Yan N (2019). Modulation of cardiac ryanodine receptor 2 by calmodulin. *Nature* **572,** 347-351.

Hwang HS, Nitu FR, Yang Y, Walweel K, Pereira L, Johnson CN, Faggioni M, Chazin WJ, Laver D, George AL, Jr., Cornea RL, Bers DM & Knollmann BC (2014). Divergent regulation of ryanodine receptor 2 calcium release channels by arrhythmogenic human calmodulin missense mutants. *Circ Res* **114,** 1114-1124.

Ikura M (1996). Calcium binding and conformational response in EF-hand proteins. *Trends Biochem Sci* **21,** 14-17.

Johnson CN, Potet F, Thompson MK, Kroncke BM, Glazer AM, Voehler MW, Knollmann BC, George AL, Jr. & Chazin WJ (2018). A Mechanism of Calmodulin Modulation of the Human Cardiac Sodium Channel. *Structure* **26,** 683-694 e683.

Kabsch W (2010). Xds. *Acta Crystallogr D Biol Crystallogr* **66,** 125-132.

Lau K, Chan MM & Van Petegem F (2014). Lobe-specific calmodulin binding to different ryanodine receptor isoforms. *Biochemistry* **53,** 932-946.

Limpitikul WB, Dick IE, Joshi-Mukherjee R, Overgaard MT, George AL, Jr. & Yue DT (2014). Calmodulin mutations associated with long QT syndrome prevent inactivation of cardiac L-type Ca(2+) currents and promote proarrhythmic behavior in ventricular myocytes. *J Mol Cell Cardiol* **74,** 115-124.

Linse S, Helmersson A & Forsen S (1991). Calcium binding to calmodulin and its globular domains. *J Biol Chem* **266,** 8050-8054.

Liu Z & Vogel HJ (2012). Structural basis for the regulation of L-type voltage-gated calcium channels: interactions between the N-terminal cytoplasmic domain and Ca(2+)-calmodulin. *Front Mol Neurosci* **5,** 38.

Makita N, Yagihara N, Crotti L, Johnson CN, Beckmann BM, Roh MS, Shigemizu D, Lichtner P, Ishikawa T, Aiba T, Homfray T, Behr ER, Klug D, Denjoy I, Mastantuono E, Theisen D, Tsunoda T, Satake W, Toda T, Nakagawa H, Tsuji Y, Tsuchiya T, Yamamoto H, Miyamoto Y, Endo N, Kimura A, Ozaki K, Motomura H, Suda K, Tanaka T, Schwartz PJ, Meitinger T, Kaab S, Guicheney P, Shimizu W, Bhuiyan ZA, Watanabe H, Chazin WJ & George AL, Jr (2014). Novel calmodulin mutations associated with congenital arrhythmia susceptibility. *Circ Cardiovasc Genet* **7,** 466-474.

Marsman RF, Barc J, Beekman L, Alders M, Dooijes D, van den Wijngaard A, Ratbi I, Sefiani A, Bhuiyan ZA, Wilde AA & Bezzina CR (2014). A mutation in CALM1 encoding calmodulin in familial idiopathic ventricular fibrillation in childhood and adolescence. *J Am Coll Cardiol* **63,** 259-266.

Masino L, Martin SR & Bayley PM (2000). Ligand binding and thermodynamic stability of a multidomain protein, calmodulin. *Protein Sci* **9,** 1519-1529.

Minowa O & Yagi K (1984). Calcium binding to tryptic fragments of calmodulin. *J Biochem* **96,** 1175-1182.

Nyegaard M, Overgaard MT, Sondergaard MT, Vranas M, Behr ER, Hildebrandt LL, Lund J, Hedley PL, Camm AJ, Wettrell G, Fosdal I, Christiansen M & Borglum AD (2012). Mutations in calmodulin cause ventricular tachycardia and sudden cardiac death. *Am J Hum Genet* **91,** 703-712.

Pancaroglu R & Van Petegem F (2018). Calcium Channelopathies: Structural Insights into Disorders of the Muscle Excitation-Contraction Complex. *Annu Rev Genet* **52,** 373-396.

Peterson BZ, DeMaria CD, Adelman JP & Yue DT (1999). Calmodulin is the Ca2+ sensor for Ca2+ -dependent inactivation of L-type calcium channels. *Neuron* **22,** 549-558.

Reed GJ, Boczek NJ, Etheridge SP & Ackerman MJ (2015). CALM3 mutation associated with long QT syndrome. *Heart Rhythm* **12,** 419-422.

Saljic A, Muthukumarasamy KM, la Cour JM, Boddum K, Grunnet M, Berchtold MW & Jespersen T (2019). Impact of arrhythmogenic calmodulin variants on small conductance Ca(2+) -activated K(+) (SK3) channels. *Physiol Rep* **7,** e14210.

Sarhan MF, Tung CC, Van Petegem F & Ahern CA (2012). Crystallographic basis for calcium regulation of sodium channels. *Proc Natl Acad Sci U S A* **109,** 3558-3563.

Sondergaard MT, Liu Y, Brohus M, Guo W, Nani A, Carvajal C, Fill M, Overgaard MT & Chen SRW (2019). Diminished inhibition and facilitated activation of RyR2-mediated Ca(2+) release is a common defect of arrhythmogenic calmodulin mutations. *FEBS J*.

Sondergaard MT, Sorensen AB, Skov LL, Kjaer-Sorensen K, Bauer MC, Nyegaard M, Linse S, Oxvig C & Overgaard MT (2015a). Calmodulin mutations causing catecholaminergic polymorphic ventricular tachycardia confer opposing functional and biophysical molecular changes. *FEBS J* **282,** 803-816.

Sondergaard MT, Tian X, Liu Y, Wang R, Chazin WJ, Chen SR & Overgaard MT (2015b). Arrhythmogenic Calmodulin Mutations Affect the Activation and Termination of Cardiac Ryanodine Receptor-mediated Ca2+ Release. *J Biol Chem* **290,** 26151-26162.

Sorensen AB, Sondergaard MT & Overgaard MT (2013). Calmodulin in a heartbeat. *The FEBS journal* **280,** 5511-5532.

Sorensen BR & Shea MA (1998). Interactions between domains of apo calmodulin alter calcium binding and stability. *Biochemistry* **37,** 4244-4253.

Sreerama N & Woody RW (2000). Estimation of protein secondary structure from circular dichroism spectra: comparison of CONTIN, SELCON, and CDSSTR methods with an expanded reference set. *Anal Biochem* **287,** 252-260.

Sun J & MacKinnon R (2017). Cryo-EM Structure of a KCNQ1/CaM Complex Reveals Insights into Congenital Long QT Syndrome. *Cell* **169,** 1042-1050 e1049.

Tsalkova TN & Privalov PL (1985). Thermodynamic study of domain organization in troponin C and calmodulin. *J Mol Biol* **181,** 533-544.

Van Petegem F (2012). Ryanodine Receptors: Structure and Function. *J Biol Chem* **287,** 31624-31632.

Van Petegem F, Chatelain FC & Minor DL, Jr (2005). Insights into voltage-gated calcium channel regulation from the structure of the CaV1.2 IQ domain-Ca2+/calmodulin complex. *Nat Struct Mol Biol* **12,** 1108-1115.

Van Petegem F, Lobo PA & Ahern CA (2012). Seeing the Forest through the Trees: towards a Unified View on Physiological Calcium Regulation of Voltage-Gated Sodium Channels. *Biophys J* **103,** 2243-2251.

VanScyoc WS & Shea MA (2001). Phenylalanine fluorescence studies of calcium binding to N-domain fragments of Paramecium calmodulin mutants show increased calcium affinity correlates with increased disorder. *Protein Sci* **10,** 1758-1768.

Wang C, Chung BC, Yan H, Lee SY & Pitt GS (2012). Crystal Structure of the Ternary Complex of a NaV C-Terminal Domain, a Fibroblast Growth Factor Homologous Factor, and Calmodulin. *Structure* **20,** 1167-1176.

Wang C, Chung BC, Yan H, Wang HG, Lee SY & Pitt GS (2014). Structural analyses of Ca(2)(+)/CaM interaction with NaV channel C-termini reveal mechanisms of calcium-dependent regulation. *Nat Commun* **5,** 4896.

Wang CL (1985). A note on Ca2+ binding to calmodulin. *Biochem Biophys Res Commun* **130,** 426-430.

Wang K, Holt C, Lu J, Brohus M, Larsen KT, Overgaard MT, Wimmer R & Van Petegem F (2018). Arrhythmia mutations in calmodulin cause conformational changes that affect interactions with the cardiac voltage-gated calcium channel. *Proc Natl Acad Sci U S A* **115,** E10556-E10565.

Whitmore L & Wallace BA (2004). DICHROWEB, an online server for protein secondary structure analyses from circular dichroism spectroscopic data. *Nucleic Acids Res* **32,** W668-673.

Wren LM, Jimenez-Jaimez J, Al-Ghamdi S, Al-Aama JY, Bdeir A, Al-Hassnan ZN, Kuan JL, Foo RY, Potet F, Johnson CN, Aziz MC, Carvill GL, Kaski JP, Crotti L, Perin F, Monserrat L, Burridge PW, Schwartz PJ, Chazin WJ, Bhuiyan ZA & George AL, Jr (2019). Genetic Mosaicism in Calmodulinopathy. *Circ Genom Precis Med* **12,** 375-385.

Yin G, Hassan F, Haroun AR, Murphy LL, Crotti L, Schwartz PJ, George AL & Satin J (2014). Arrhythmogenic calmodulin mutations disrupt intracellular cardiomyocyte Ca2+ regulation by distinct mechanisms. *J Am Heart Assoc* **3,** e000996.

Yoder JB, Ben-Johny M, Farinelli F, Srinivasan L, Shoemaker SR, Tomaselli GF, Gabelli SB & Amzel LM (2019). Ca(2+)-dependent regulation of sodium channels NaV1.4 and NaV1.5 is controlled by the post-IQ motif. *Nat Commun* **10,** 1514.

Zheng H, Cooper DR, Porebski PJ, Shabalin IG, Handing KB & Minor W (2017). CheckMyMetal: a macromolecular metal-binding validation tool. *Acta Crystallogr D Struct Biol* **73,** 223-233.

Zuhlke RD, Pitt GS, Deisseroth K, Tsien RW & Reuter H (1999). Calmodulin supports both inactivation and facilitation of L-type calcium channels. *Nature* **399,** 159-162.

## ADDITIONAL INFORMATION

### COMPETING INTERESTS

The authors declare that they have no competing interests.

### AUTHOR CONTRIBUTIONS

KW performed all crystallographic studies and wrote the manuscript. MB performed the CD and TAMRA experiments, supervised by MO. RW and CH performed the NMR experiments. FVP defined the project and wrote parts of the manuscript. All authors contributed to editing and approval of the final manuscript version. The authors agree to be accountable for all aspects of the work.

### FUNDING

FVP acknowledges a grant from the CIHR (PJT 148632). RW and CH acknowledge a grant from the NovoNordisk Foundation (NNF18OC0053032). MTO was supported by research grants from the Obelske Family Foundation, the Novo Nordic Foundation (NNF15OC0012345, NNF16OC0023344), the Lundbeck Foundation (R151-2013-14432), and the Danish Council for Independent Research (DFF-4181-00447).

### ACKNOWLEDGEMENTS

We thank the support staff at the Advanced Photon Source (Chicago) GM/CA-CAT beamline 23-ID-D, the Stanford Synchrotron Radiation Lightsource (Menlo Park, USA), and at the Canadian Light Source (Saskatoon, SK, Canada), which is supported by the Natural Sciences and Engineering Research Council of Canada, the National Research Council Canada, the Canadian Institutes of Health Research (CIHR), the Province of Saskatchewan, Western Economic Diversification Canada, and the University of Saskatchewan. The NMR laboratory at Aalborg University is supported by the Obel Family, the Carlsberg and SparNord foundations.

**Table 1 Data collection and refinement statistics (molecular replacement)**

| | D130G $Ca^{2+}$/CaM:IQ domain | N98S $Ca^{2+}$/CaM:IQ domain | Q136P $Ca^{2+}$/CaM:IQ domain | N54I $Ca^{2+}$/CaM:IQ domain |
|---|---|---|---|---|
| **Data collection** | | | | |
| Space group | $P2_12_12$ | $P2_12_12_1$ | $P2_122_1$ | $P2_1$ |
| Cell dimensions | | | | |
| *a*, *b*, *c* (Å) | 121.8, 161.6, 96.3 | 63.4, 68.1, 86.3 | 41.6, 56.6, 68.6 | 59.4, 43.4, 67.0 |
| α, β, γ (°) | 90.0, 90.0, 90.0 | 90.0, 90.0, 90.0 | 90.0, 90.0, 90.0 | 90.0, 111.9, 90.0 |
| Resolution (Å) | 50.0-2.30 (2.44-2.30) | 50.0-1.65 (1.75-1.65) | 40.0-1.70 (1.80-1.70) | 50.0-1.75 (1.86-1.75) |
| $R_{merge}$ (%) | 3.1 (48.6) | 4.5 (51.8) | 12.1 (100.1) | 3.9 (25.5) |
| $R_{meas}$ (%) | 3.8 (58.8) | 5.4 (63.0) | 12.8 (105.3) | 5.3 (34.9) |
| $I/\sigma(I)$ | 17.06 (2.11) | 13.50 (2.06) | 16.32 (2.22) | 11.55 (2.51) |
| $CC_{1/2}$ | 99.9 (79.9) | 99.9 (81.3) | 99.9 (74.2) | 99.7 (88.3) |
| Completeness (%) | 97.5 (97.6) | 98.6 (98.4) | 99.9 (99.9) | 89.6 (69.0) |
| Redundancy | 2.93 (2.98) | 2.93 (2.94) | 10.61 (10.39) | 1.72 (1.44) |
| **Refinement** | | | | |
| Resolution (Å) | 49.04-2.40 | 35.66-1.65 | 35.58-1.70 | 35.56-1.75 |
| No. reflections | 140090 | 85568 | 18437 | 56089 |
| $R_{work}$ / $R_{free}$ | 23.18/28.27 | 17.80/20.88 | 17.12/20.04 | 16.36/20.09 |
| No. atoms | | | | |
| Protein | 11328 | 2734 | 1450 | 2766 |
| Ligand | 29 | 9 | 5 | 8 |
| Water | 20 | 301 | 159 | 217 |
| *B* factors | | | | |
| Protein | 85.5 | 32.0 | 17.8 | 28.8 |
| Ligand | 82.3 | 24.6 | 14.4 | 22.3 |
| Water | 68.0 | 36.5 | 28.0 | 35.0 |

| | | | | |
|---|---|---|---|---|
| R.m.s. deviations | | | | |
| Bond lengths (Å) | 0.002 | 0.006 | 0.006 | 0.006 |
| Bond angles (°) | 0.371 | 0.745 | 0.760 | 0.735 |

One crystal was used for each structure solution. Highest resolution shell is shown in parentheses.

**Figure 1** Binding and structural analysis of arrhythmogenic CaM mutants. (A) Binding affinity ($K_{D,app}$) of full-length CaM variants for the $Ca_V1.2$ IQ domain at various free $Ca^{2+}$ concentrations by TAMRA fluorescence anisotropy. Error bars represent the standard deviation of three replicates. (B) Circular dichroism (CD) spectra of two $Ca^{2+}$-free CaM variants. Smooth lines represent the mean and error bars represent the standard deviation of four replicates. CD spectra of $Ca^{2+}$-saturated CaM variants, showing the overall spectrum (C) and a zoom (D) at 222 nm and 208 nm. Error bars represent the standard deviation of four replicates.

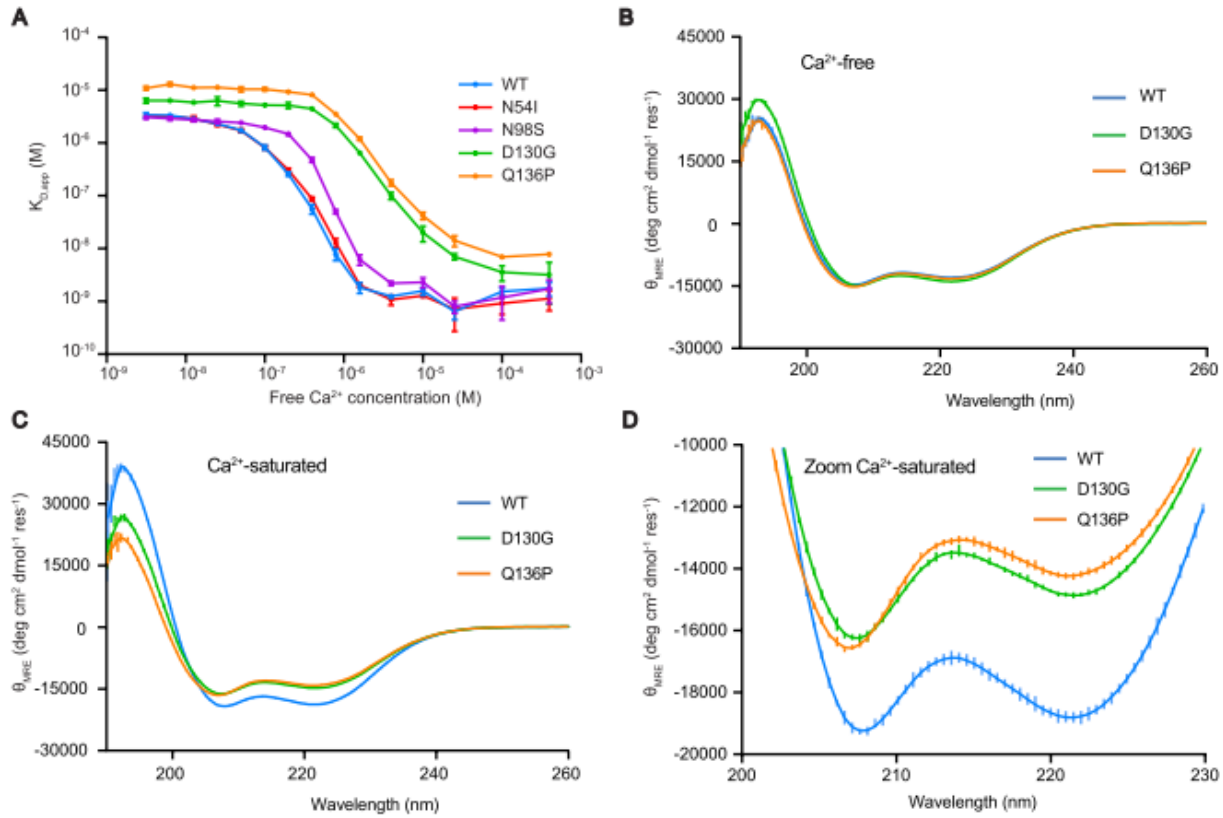

**Figure 2** Comparisons of WT and D130G CaM structures, obtained under saturating $Ca^{2+}$ concentrations (10 mM $CaCl_2$). Stick representations of EF4 of (A) WT $Ca^{2+}$/CaM (PDB ID code 3G43), (B) D130G $Ca^{2+}$/CaM (chain K), (C) D130G $Ca^{2+}$/CaM (chain M), and (D) WT apoCaM (PDB ID code 1QX5). The conformation of EF4 is thus different from both WT apoCaM and $Ca^{2+}$/CaM. Residue 130 is shown in black and the $Ca^{2+}$ ion as a sphere. Selected residues are labelled. (E) Superposition of the C-lobes of WT $Ca^{2+}$/CaM (white) and D130G $Ca^{2+}$/CaM (blue) based on helix E. C-lobes are shown in ribbon representation; helices are labelled. EF hands 3 and 4 have completely unraveled in the mutant.

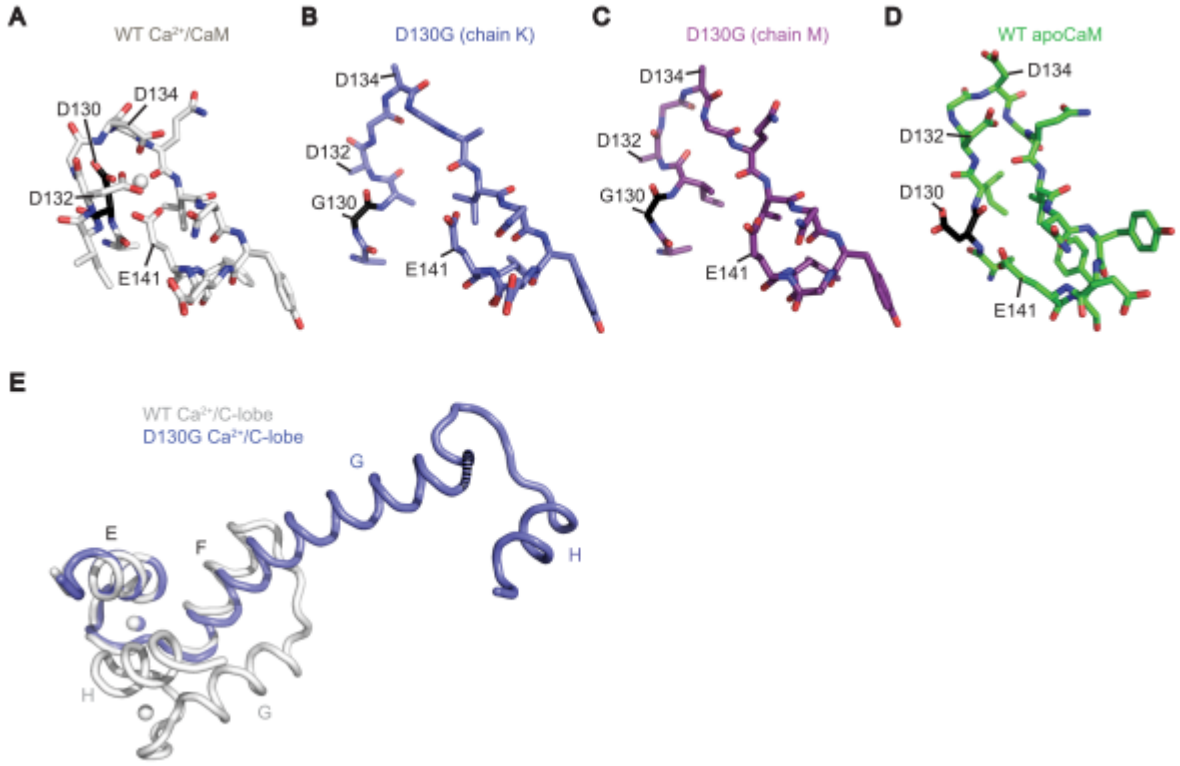

**Figure 3** The D130G $Ca^{2+}$/CaM:IQ domain complex forms a dimer in the crystal structure but not in solution. (A) Dimeric D130G $Ca^{2+}$/CaMs (cartoon: blue, purple) bound to IQ domains (sticks: orange, beige) as seen in the crystal structure. $Ca^{2+}$ ions are shown as spheres; helices are labelled. (B) Zoom of residues at the dimer interface; selected residues are shown in sticks and labelled. (C) Chromatogram of the WT and D130G $Ca^{2+}$/CaM:IQ complexes passed through a gel filtration column.

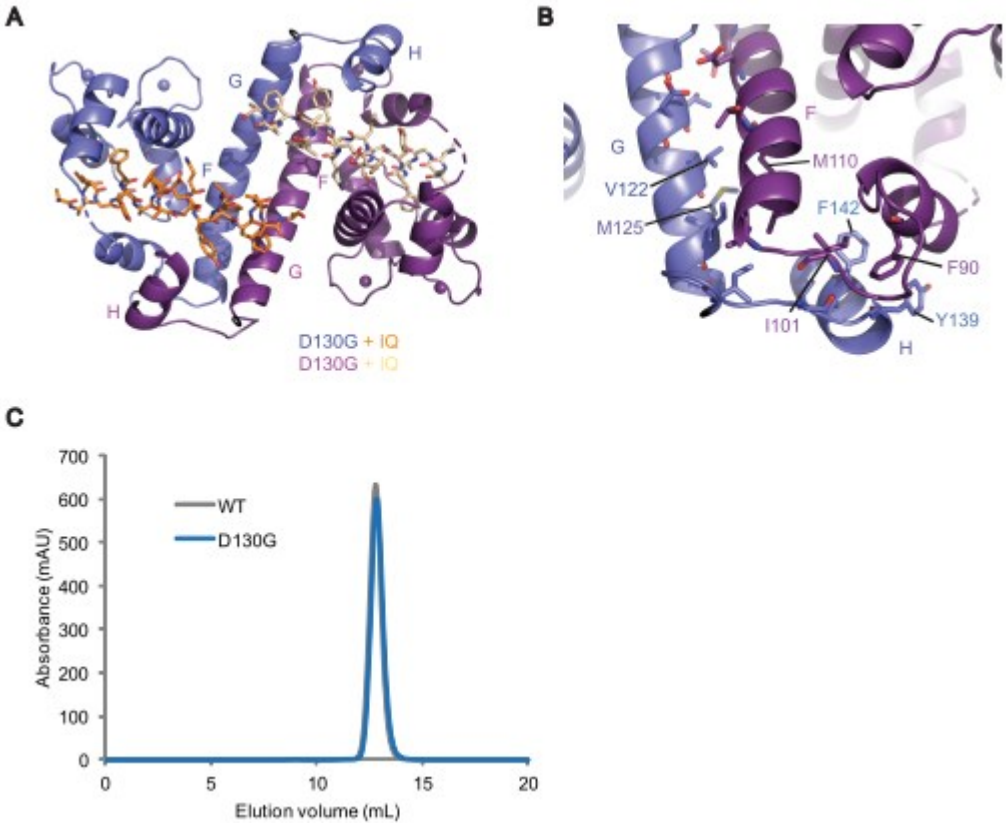

**Figure 4** Comparisons of WT and D130G $Ca^{2+}$/CaM interactions with the IQ domain. Interactions of (A) WT (PDB ID code 3G43) and (B) D130G $Ca^{2+}$/CaM with the IQ domain. The IQ domain is shown in stick representation; CaM is shown in surface representation with the colors indicating electrostatic potential (red: negative; blue: positive). Zoom of (C) WT and (D) D130G C-lobe interactions with the IQ domain. Selected residues are shown in sticks under the transparent surface. Residue labels in the IQ domain are boxed.

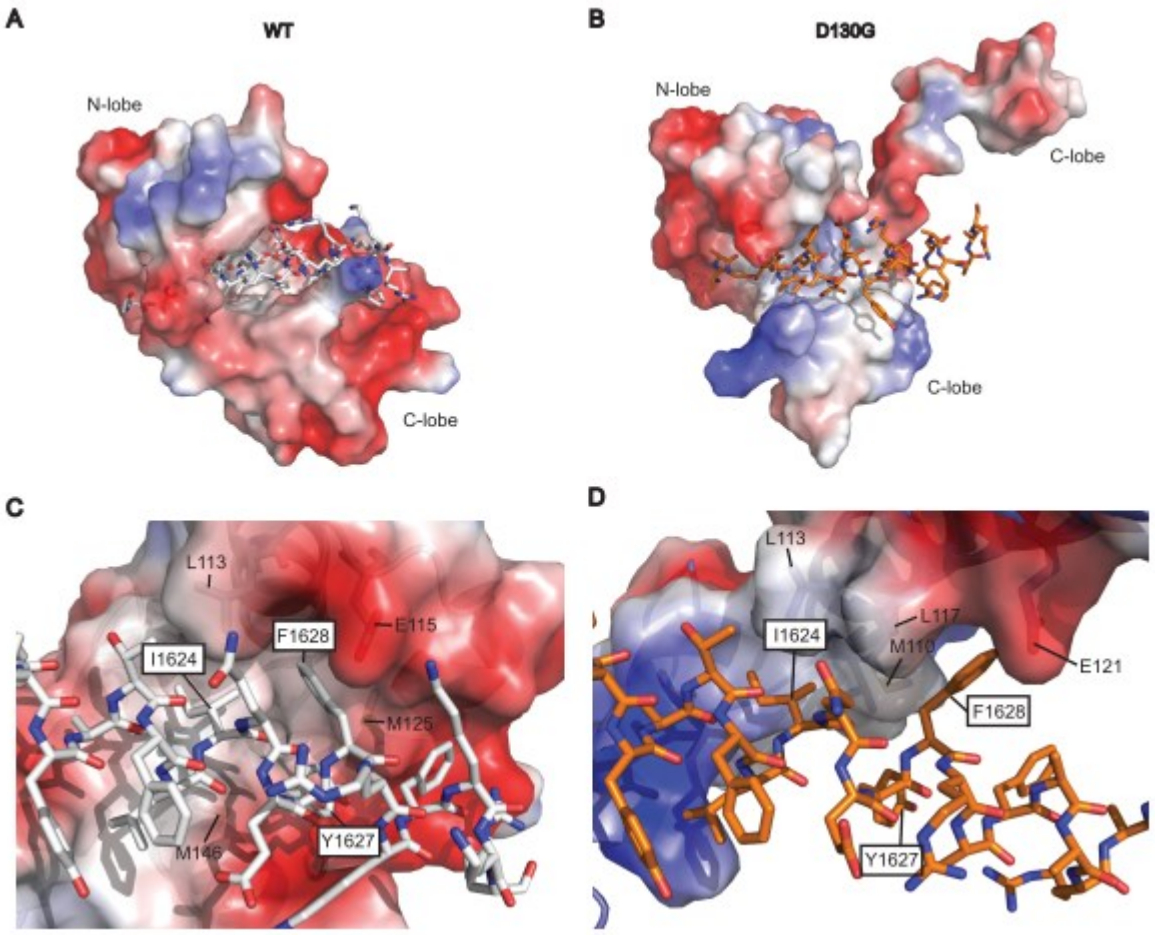

**Figure 5** Comparisons of WT and Q136P $Ca^{2+}$/CaM:IQ domain structures, obtained under saturating $Ca^{2+}$ concentrations (10 mM $CaCl_2$). (A) Superpositions of EF4 of WT (PDB ID code 2BE6, white) and Q136P $Ca^{2+}$/CaM (blue). EF4 is shown in stick representation, P136 in black, and $Ca^{2+}$ ions as spheres. (B) Zoomed and rotated view around the Q136P mutation site. (C) Superpositions of the WT and Q136P C-lobes, shown around residue Y99. Interactions of C-lobes of (D) WT and (E) Q136P with the IQ domain. The IQ domain is shown in stick representation; C-lobes are shown in surface representation with the colors indicating electrostatic potential (red: negative; blue: positive); selective residues are shown in sticks under the transparent surface. Residue labels in the IQ domain are boxed.

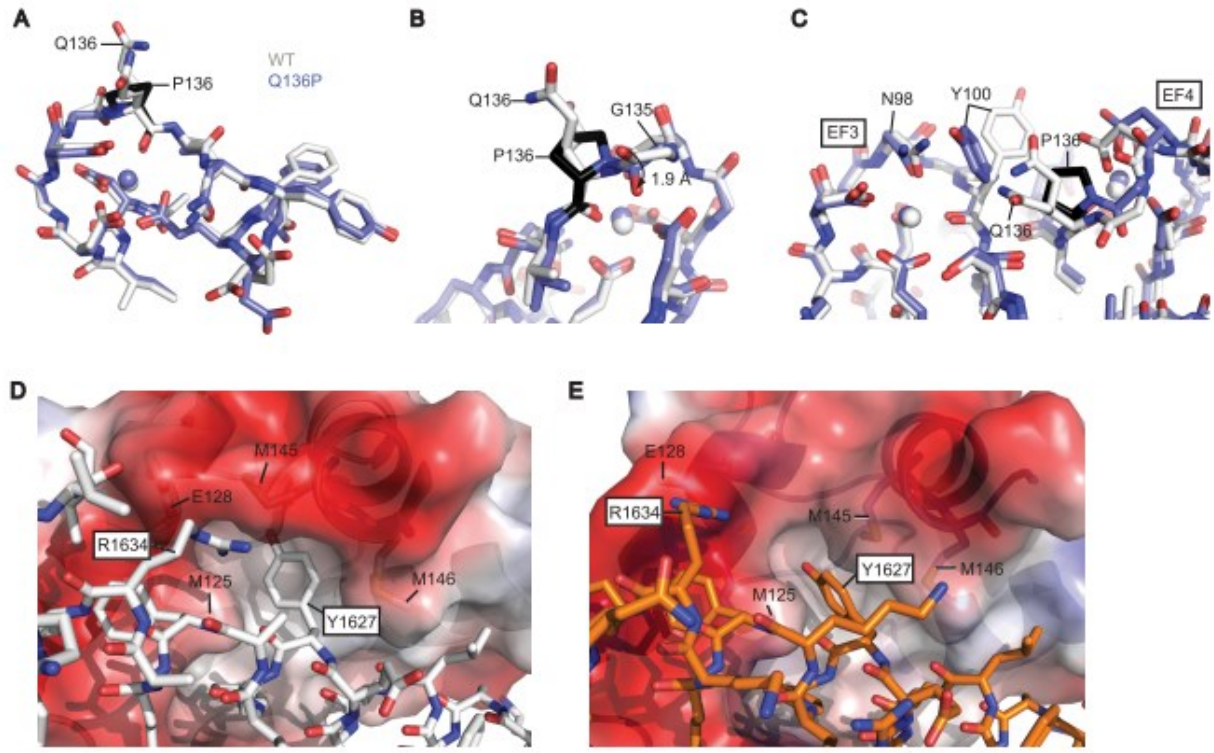

**Figure 6** Comparisons of WT and N98S (chain B) $Ca^{2+}$/CaM:IQ structures. The N98S structure was solved at a free $Ca^{2+}$ concentration of ~10 μM. Stick representations of EF3 of (A) WT (PDB ID code 2BE6) and (B) N98S (chain B) $Ca^{2+}$/CaM. Residue 98 is shown in black and $Ca^{2+}$ ions as spheres. (C) Overall superposition of the C-lobes of WT (white) and N98S (chain B, blue) $Ca^{2+}$/CaM. C-lobes are shown in ribbon representation; helices are labelled. (D) Superposition of WT (white) and N98S (chain B, N-lobe in green, C-lobe in blue) $Ca^{2+}$/CaM:IQ based on the IQ domain (the IQ domain bound to the N98S mutant is orange). CaM is shown in cartoon representation and IQ domain as sticks.

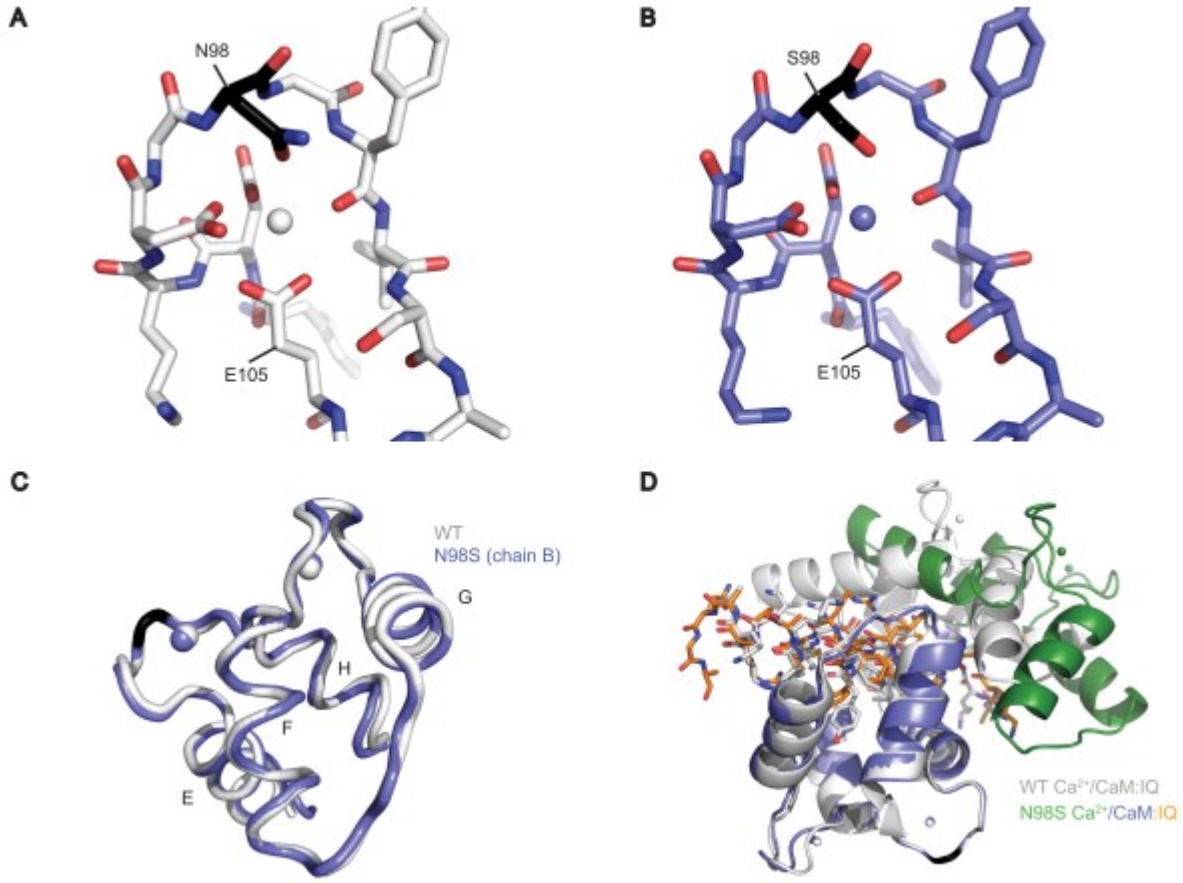

**Figure 7** Comparisons of WT, N98I, and N98S (chain A) $Ca^{2+}$/CaM:IQ structures. N98I was previously solved under saturating $Ca^{2+}$ levels (10 mM $CaCl_2$) (Wang *et al.*, 2018), whereas N98S here crystallized at 10 μM free $Ca^{2+}$. Stick representations of EF3 of (A) N98I (PDB ID code 6DAD) and (B) N98S (chain A) $Ca^{2+}$/CaM. Residue 98 is shown in black, $Na^{+}$ ion as a purple sphere, and water molecules as red spheres. (C) Superposition of C-lobes of WT (PDB ID code 2BE6, white) and N98S (chain A, blue) $Ca^{2+}$/CaM based on helix E. C-lobes are shown in ribbon representation, residue 98 in black, $Na^{+}$ ion as a purple sphere, and $Ca^{2+}$ ions as white/blue spheres; helices are labelled. (D) Superposition of WT (white) and N98S (chain A, N-lobe in green, C-lobe in blue) $Ca^{2+}$/CaM:IQ based on the IQ domain (IQ of N98S mutant is orange). CaM is shown in cartoon representation and IQ domain as sticks.

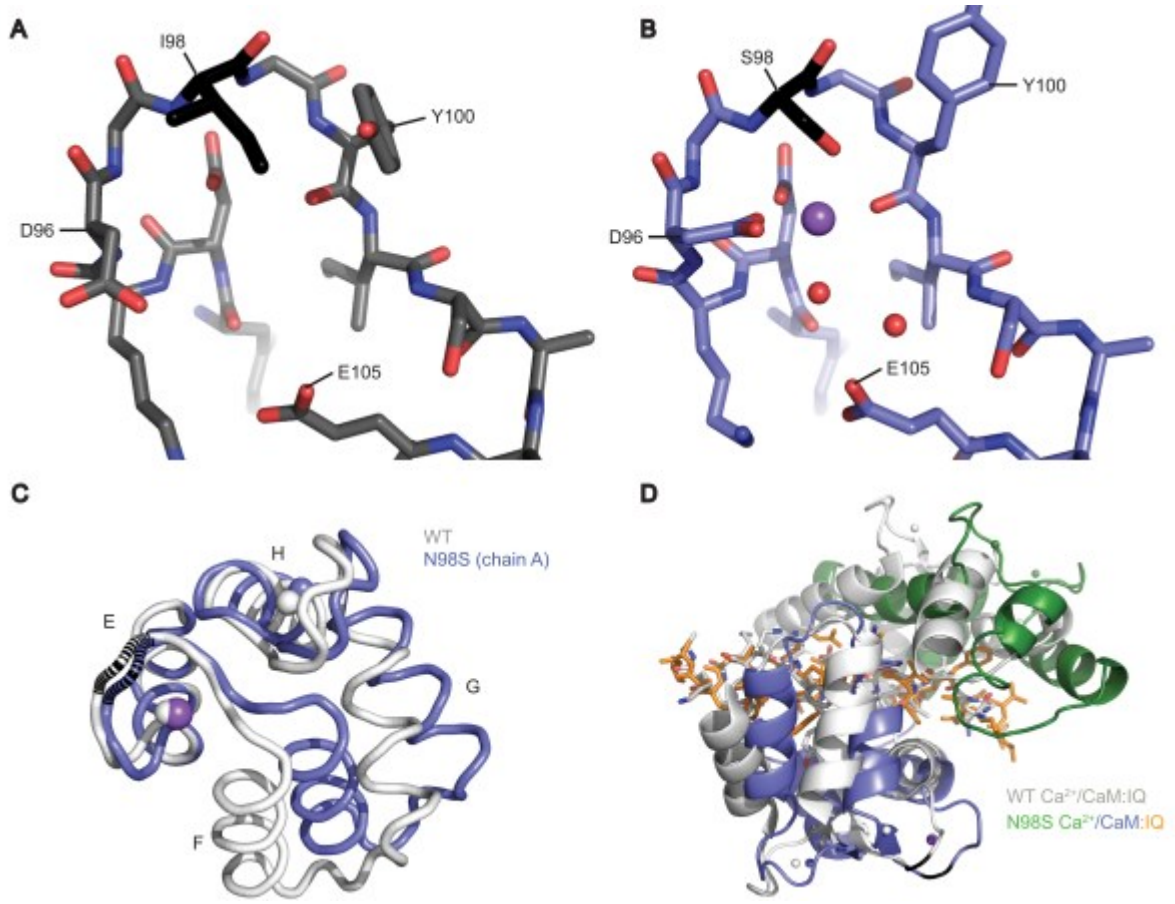

**Figure 8** Comparisons of WT, N98I, and N98S (chain A) $Ca^{2+}$/CaM:IQ structures. N98I was previously solved under saturating $Ca^{2+}$ levels (10 mM $CaCl_2$) (Wang *et al.*, 2018), whereas N98S here crystallized at 10 μM free $Ca^{2+}$. (A) Superpositions of EF3 of WT (PDB ID code 2BE6, white), N98I (PDB ID code 6DAD, gray), and N98S (chain A, blue) $Ca^{2+}$/CaM. EF3 is shown in stick representation, residue 98 in black, $Na^+$ ion as a purple sphere, and $Ca^{2+}$ ions as gray/blue spheres. (B) Overall superposition of the C-lobes of N98I (gray) and N98S (chain A, blue) $Ca^{2+}$/CaM. C-lobes are shown in ribbon representation; helices are labelled. (C) Superpositions of N98I (gray) and N98S (chain A, N-lobe in green, C-lobe in blue) $Ca^{2+}$/CaM based on the IQ domain (IQ of N98S mutant is orange). CaM is shown in cartoon representation and IQ domain as sticks.

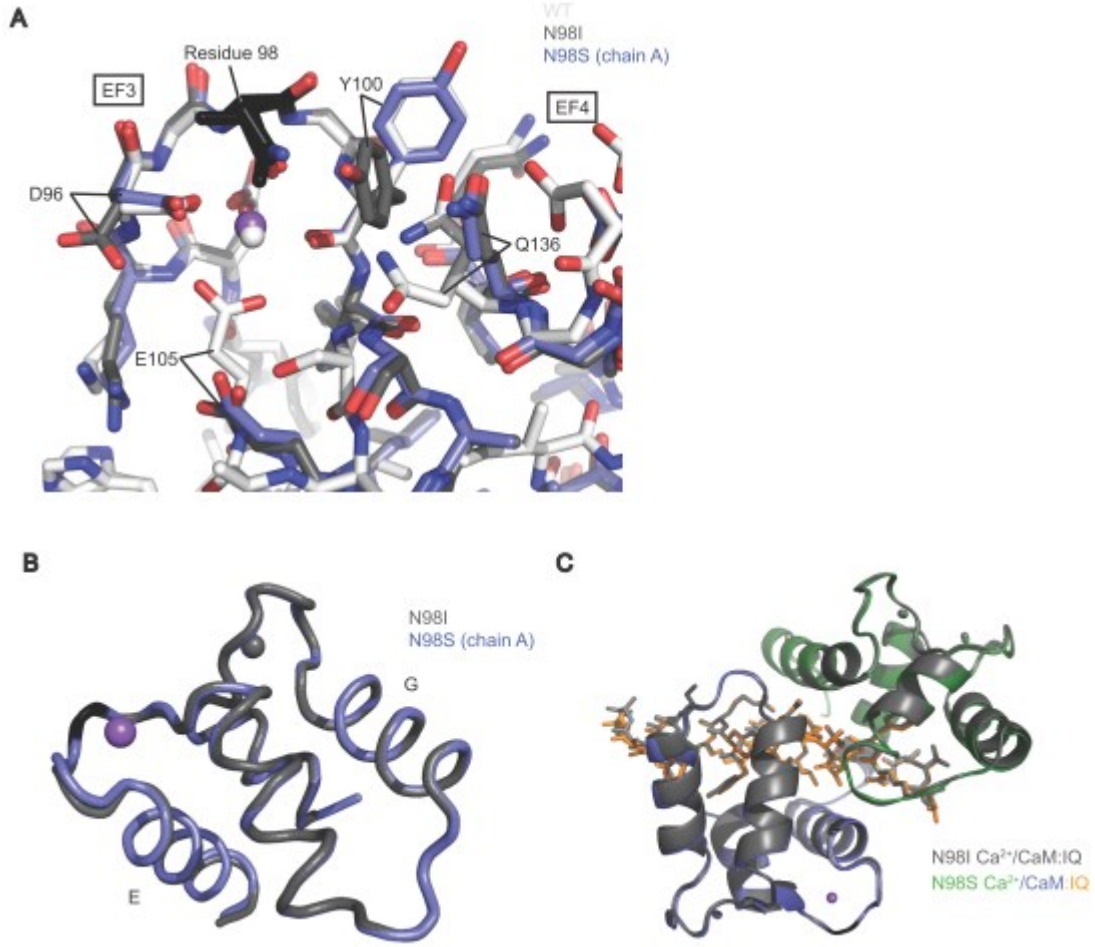

**Figure 9** Overlay of [$^{1}$H-$^{15}$N]-HSQC spectra of the $Ca^{2+}$-loaded form of CaM bound to the $Ca_V1.2$ IQ peptide. All experiments were performed under saturating $Ca^{2+}$ concentrations (1 mM $CaCl_2$). Chemical shifts for WT CaM are shown in black, N98S CaM in red. The left panel shows the entire spectrum, and the right shows a zoom.

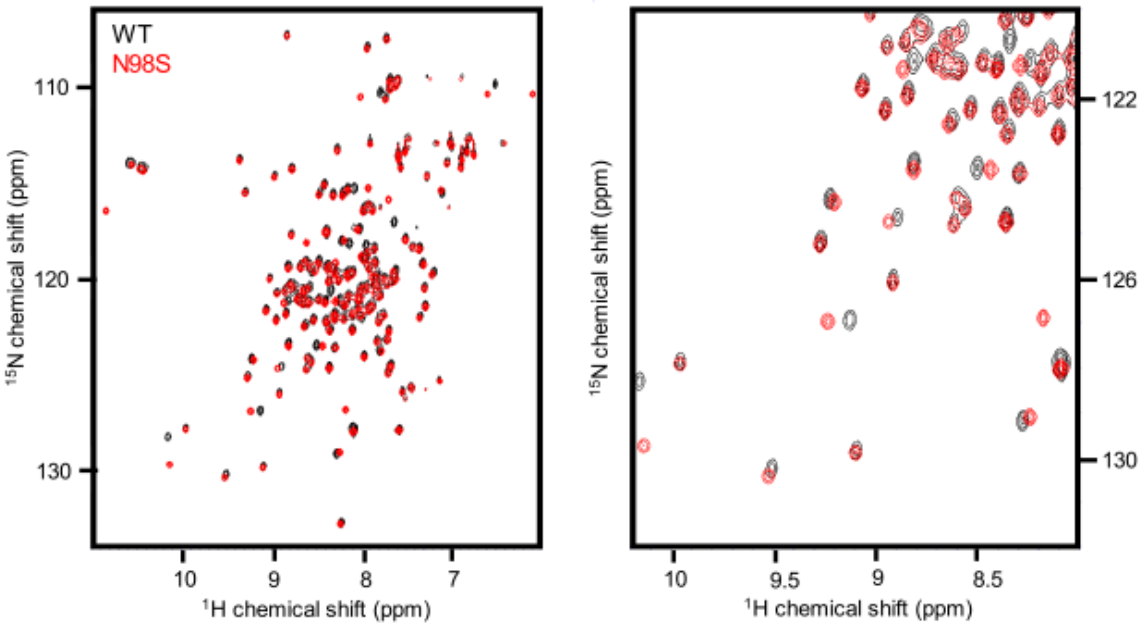

**Figure 10** Overlay of [$^{1}$H-$^{15}$N]-HSQC spectra of $Ca^{2+}$-saturated CaM variants bound to the $Ca_V1.2$ IQ domain (all at 1 mM $CaCl_2$): WT CaM is shown in black, D96V in blue, and N98S in red. The left panels show the entire spectrum, and the right panels show a zoomed in region.

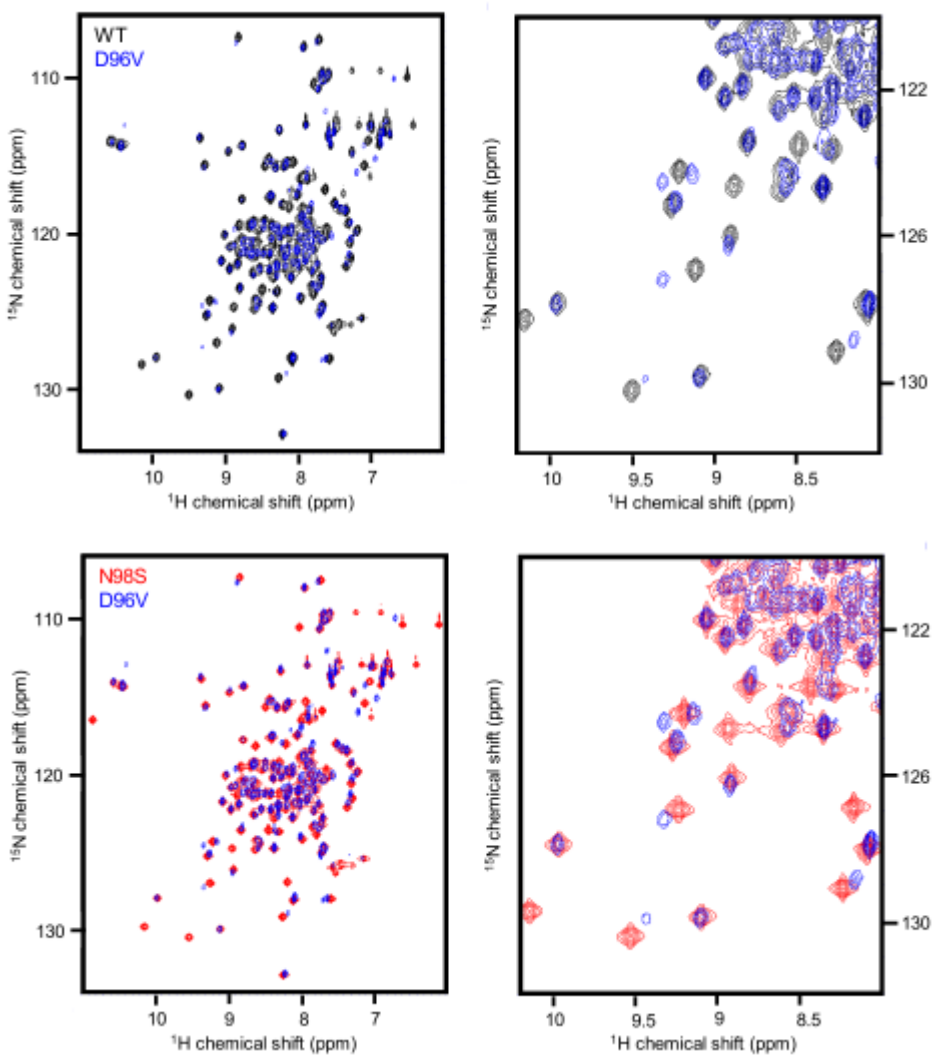

**Figure 11** Comparisons of WT and N54I $Ca^{2+}$/CaM:IQ structures, obtained under saturating $Ca^{2+}$ concentrations (10 mM $CaCl_2$). (A) Superposition of WT (PDB ID code 3G43, white) and N54I (N-lobe in green, C-lobe in blue) $Ca^{2+}$/CaM based on the IQ domain (IQ of N54I mutant is orange). CaM is shown in cartoon representation, IQ domain as sticks, and $Ca^{2+}$ ions as spheres. (B) Overall superposition of the N-lobes of WT (white) and N54I (green) $Ca^{2+}$/CaM. N-lobes are shown in ribbon representation and I54 in black; helices are labelled. (C) Superposition of helix C of the WT and N54I N-lobes, shown in stick representation.

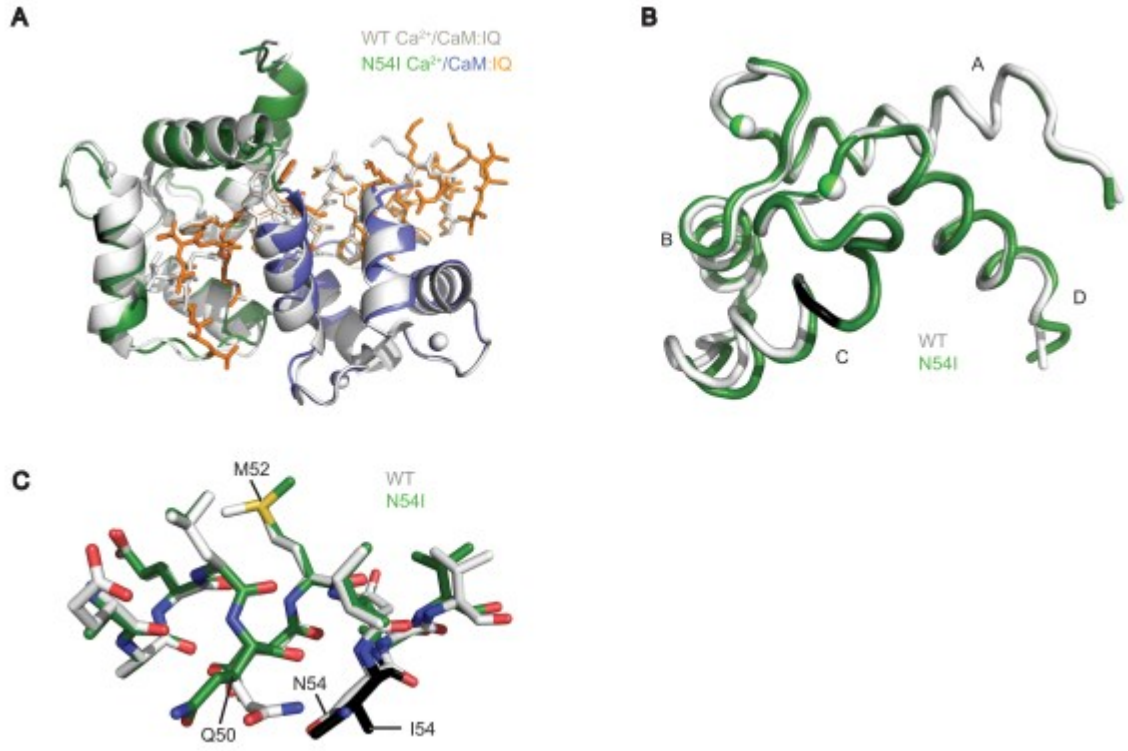


**Author profile**

Kaiqian Wang is a PhD candidate in the Biochemistry and Molecular Biology graduate program at The University of British Columbia and works in the laboratory of Filip Van Petegem. Her work focuses on understanding the mechanism by which arrhythmogenic calmodulin mutations cause disease from a structural and biophysical perspective. She is interested in investigating the functional regulation of ion channels in health and disease.